Pseudogap and high-temperature superconductivity from weak to strong coupling. Towards quantitative theory

(Review Article)

A.-M.S. Tremblay, B. Kyung, and D. Sénéchal

Département de Physique and RQMP, Université de Sherbrooke, Sherbrooke, QC J1K 2R1, Canada
E-mail: tremblay@physique.usherbrooke.ca

This is a short review of the theoretical work on the two-dimensional Hubbard model performed in Sherbrooke in the last few years. It is written on the occasion of the twentieth anniversary of the discovery of high-temperature superconductivity. We discuss several approaches, how they were benchmarked and how they agree sufficiently with each other that we can trust that the results are accurate solutions of the Hubbard model. Then comparisons are made with experiment. We show that the Hubbard model does exhibit d-wave superconductivity and antiferromagnetism essentially where they are observed for both hole and electron-doped cuprates. We also show that the pseudogap phenomenon comes out of these calculations. In the case of electron-doped high temperature superconductors, comparisons with angle-resolved photoemission experiments are nearly quantitative. The value of the pseudogap temperature observed for these compounds in recent photoemission experiments has been predicted by theory before it was observed experimentally. Additional experimental confirmation would be useful. The theoretical methods that are surveyed include mostly the two-particle self-consistent approach, variational cluster perturbation theory (or variational cluster approximation), and cellular dynamical mean-field theory.

1. Introduction

In the first days of the discovery of high-temperature superconductivity, Anderson [1] suggested that the two-dimensional Hubbard model held the key to the phenomenon. Despite its apparent simplicity, the two-dimensional Hubbard model is a formidable challenge for theorists. The dimension is not low enough that an exact solution is available, as in one dimension. The dimension is not high enough that some mean-field theory, like dynamical mean field theory (DMFT) [2,3], valid in infinite dimension, can come to the rescue. In two dimensions, both quantum and thermal fluctuations are important. In addition, as we shall see, it turns out that the real materials are in a situation where both potential and kinetic energy are comparable. We cannot begin with the wave picture (kinetic energy dominated, or so-called «weak coupling») and do perturbation theory, and we cannot begin from the particle picture (potential energy dominated, or so-called «strong coupling») and do perturbation theory. In fact, even if one starts from the wave picture, perturbation theory is not trivial in two dimensions, as we shall see. Variational approaches on the ground state have been proposed [4], but even if they capture key aspects of the ground state, they say little about one-particle excitations.

Even before the discovery of high-temperature superconductivity, it was suggested that antiferromagnetic fluctuations present in the Hubbard model could lead to d-wave superconductivity [5–7], a sort of generalization of the Kohn–Luttinger mechanism [8] analogous to the superfluidity mediated by ferromagnetic spin fluctuations in ^{3}He [9]. Nevertheless,
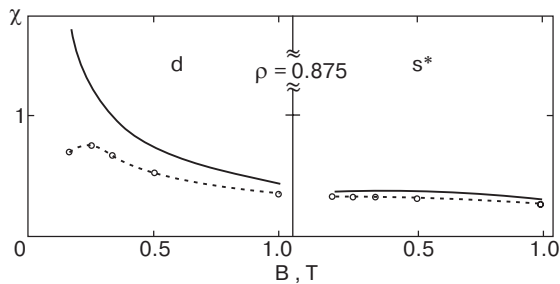
Fig. 1. The $d_{x^2-y^2}$ and extended *s*-wave susceptibilities obtained from QMC simulations for $U = 4t$ and a 4×4 lattice. The solid lines are the non-interacting results. From Ref. 10.

early quantum Monte Carlo (QMC) simulations [10] gave rather discouraging results, as illustrated in Fig. 1. In QMC, low temperatures are inaccessible because of the sign problem. At accessible temperatures, the *d*-wave pair susceptibility is smaller than the non-interacting one, instead of diverging. Since the observed phenomenon appears at temperatures that are about ten times smaller than what is accessible with QMC, the problem was left open. Until very recently then, numerical methods suggested the absence of *d*-wave superconductivity in the Hubbard model [11], despite the fact that slave-boson approaches [12,13] and many subsequent work suggested otherwise. This situation is changing since more recent variational [4], dynamical cluster approximation [14] and exact diagonalization [15] results now point towards the existence of *d*-wave superconductivity in the Hubbard model. Even more recently, new numerical approaches are making an even more convincing case [16–18].

After twenty years, we should be as quantitative as possible. How should we proceed to investigate a model without a small parameter? We will try to follow this path: 1). Identify important physical principles and laws to constrain non-perturbative approximation schemes, starting from both weak (kinetic energy dominated) and strong (potential energy dominated) coupling. 2). Benchmark the various approaches as much as possible against exact (or numerically accurate) results. 3). Check that weak and strong coupling approaches agree at intermediate coupling. 4). Compare with experiment.

In brief, we are trying to answer the question: «Is the Hubbard model rich enough to contain the essential physics of the cuprates, both hole and electron doped?» The answer is made possible by new theoretical approaches, increased computing power, and the reassurance that theoretical approaches, numerical and analytical, give consistent results at intermediate coupling even if the starting points are very different.

This paper is a review of the work we have done in Sherbrooke on this subject. In the short space provided, this review will not cover all of our work. Needless to say, we will be unfair to the work of many other groups, even though we will try to refer to the work of others that is directly relevant to ours. We do not wish to make priority claims and we apologize to the authors that may feel unfairly treated.

Section 2 will introduce the methodology: first a method that is valid at weak to intermediate coupling, the two-particle self-consistent approach (TPSC), and then various quantum cluster methods that are better at strong coupling, namely cluster perturbation theory (CPT), the variational cluster approximation (VCA) also known as variational cluster perturbation theory (VCPT), and cellular dynamical mean field theory (CDMFT) with a brief mention of the dynamical cluster approximation (DCA). In all cases, we will mention the main comparisons with exact or numerically accurate results that have been used to benchmark the approaches. In Sec. 3 we give some of the results, mostly on the pseudogap and the phase diagram of high-temperature superconductors. More importantly perhaps, we show the consistency of the results obtained by both weak- and strong-coupling approaches when they are used at intermediate coupling. Finally, we compare with experiment in Sec. 4.

2. Methodology

We consider the Hubbard model

$$H = -\sum_{i,j,\sigma} t_{ij} c_{i\sigma}^{\dagger} c_{j\sigma} + U \sum_i n_{i\uparrow} n_{i\downarrow}, \qquad (1)$$

where $c_{i\sigma}^{\dagger}$ ($c_{i\sigma}$) are creation and annihilation operators for electrons of spin σ, $n_{i\sigma} = c_{i\sigma}^{\dagger} c_{i\sigma}$ is the density of spin σ electrons, $t_{ij} = t_{ji}^{*}$ is the hopping amplitude, and U is the on-site Coulomb repulsion. In general, we write t, t', t'' respectively for the first-, second- and third-nearest neighbor hopping amplitudes.

In the following subsections, we first discuss how to approach the problem from the weak coupling perspective and then from the strong coupling point of view. The approaches that we will use in the end are non-perturbative, but in general they are more accurate either at weak or strong coupling.

2.1. Weak coupling approach

Even at weak coupling, the Hubbard model presents difficulties specific to two dimensions. The time-honored random phase approximation (RPA) has the advantage of satisfying conservation laws, but it violates the Pauli principle and the Mermin–Wag-

ner−Hohenberg−Coleman (or Mermin−Wagner, for short) theorem. This theorem states that a continuous symmetry cannot be broken at finite temperature in two dimensions. RPA gives a finite-temperature phase transition. The Pauli principle means, in particular, that $\langle n_{i\uparrow} n_{i\uparrow} \rangle = \langle n_{i\uparrow} \rangle$ in a model with only one orbital per site. This is violated by RPA since it can be satisfied only if all possible exchanges of electron lines are allowed (more on this in the following section). Since the square of the density at a given site is given by $\langle (n_{i\uparrow} + n_{i\downarrow})^2 \rangle = 2\langle n_\uparrow n_\uparrow \rangle + 2\langle n_\uparrow n_\downarrow \rangle$, violating the Pauli condition $\langle n_{i\uparrow} n_{i\uparrow} \rangle = \langle n_{i\uparrow} \rangle$ will in general lead to large errors in double occupancy, a key quantity in the Hubbard model since it is proportional to the potential energy. Another popular approach is the Moriya [19] self-consistent spin-fluctuation approach [20] that uses a Hubbard−Stratonovich transformation and a $\langle \varphi^4 \rangle \sim \varphi^2 \langle \varphi^2 \rangle$ factorization. This satisfies the Mermin−Wagner theorem but, unfortunately, violates the Pauli principle and introduces an unknown mode-coupling constant as well as an unknown renormalized U in the second-order term. The conserving approximation known as fluctuation exchange (FLEX) approximation [21] is an Eliashberg-type theory that is conserving but violates the Pauli principle, assumes a Migdal theorem and does not reproduce the pseudogap phenomenon observed in QMC. More detailed criticism of this and other approaches may be found in Refs. 22,23. Finally, the renormalization group [24−28] has the great advantage of being an unbiased method to look for instabilities towards various ordered phases. However, it is quite difficult to implement in two dimensions because of the proliferation of coupling constants, and, to our knowledge, no one has yet implemented a two-loop calculation without introducing additional approximations [29,30]. Such a two-loop calculation is necessary to observe the pseudogap phenomenon.

2.1.1. Two-particle self-consistent approach

The two-particle self-consistent (TPSC) approach, originally proposed by Vilk, Tremblay and collaborators [31,32], aims at capturing non-perturbative effects. It does not use perturbation theory or, if you want, it drops diagrammatic expansions. Instead, it is based on imposing constraints and sum rules: the theory should satisfy (a) the spin and charge conservation laws (b) the Pauli principle in the form $\langle n_{i\uparrow} n_{i\uparrow} \rangle = \langle n_{i\uparrow} \rangle$ (c) the local-moment and the local-density sum rules. Without any further explicit constraint, we find that the theory satisfies the Mermin−Wagner theorem, that it satisfies consistency between one- and two-particle quantities in the sense that $1/2 \, \mathrm{Tr} \, (\Sigma G) = U\langle n_\uparrow n_\downarrow \rangle$ and finally that the theo-

ry contains the physics of Kanamori−Brückner screening (in other words, scattering between electrons and holes includes T-matrix quantum fluctuation effects beyond the Born approximation).

Several derivations of our approach have been given [31,33], including a quite formal one [34] based on the functional derivative Baym−Kadanoff approach [35]. Here we only give an outline [36] of the approach with a more phenomenological outlook. We proceed in two steps. In the first step (in our earlier work sometimes called zeroth step), the self-energy is obtained by a Hartree−Fock-type factorization of the four-point function with the *additional constraint* that the factorization is exact when all space-time coordinates coincide [37]. Functional differentiation, as in the Baym−Kadanoff approach [35], then leads to a momentum- and frequency-independent irreducible particle-hole vertex for the spin channel that satisfies [32] $U_{sp} = U\langle n_\uparrow n_\downarrow \rangle / (\langle n_\uparrow \rangle \langle n_\downarrow \rangle)$. The local moment sum rule and the Pauli principle in the form $\langle n_\sigma^2 \rangle = \langle n_\sigma \rangle$ then determine double occupancy and U_{sp}. The irreducible vertex for the charge channel is too complicated to be computed exactly, so it is assumed to be constant and its value is found from the Pauli principle and the local charge fluctuation sum rule. To be more specific, let us use the notation, $q = (\mathbf{q}, iq_n)$ and $k = (\mathbf{k}, ik_n)$ with iq_n and ik_n respectively bosonic and fermionic Matsubara frequencies. We work in units where k_B, $\hbar$, and lattice spacing are all unity. The spin and charge susceptibilities now take the form

$$\chi_{sp}^{-1}(q) = \chi_0(q)^{-1} - \frac{1}{2}U_{sp} \tag{2}$$

and

$$\chi_{ch}^{-1}(q) = \chi_0(q)^{-1} + \frac{1}{2}U_{ch} \tag{3}$$

with χ_0 computed with the Green function $G_\sigma^{(1)}$ that contains the self-energy whose functional differentiation gave the vertices. This self-energy is constant, corresponding to the Hartree−Fock-type factorization [38]. The susceptibilities thus satisfy conservation laws [35]. One enforces the Pauli principle $\langle n_\sigma^2 \rangle = \langle n_\sigma \rangle$ implicit in the following two sum rules,

$$\frac{T}{N}\sum_q \chi_{sp}(q) = \langle (n_\uparrow - n_\downarrow)^2 \rangle = n - 2\langle n_\uparrow n_\downarrow \rangle \tag{4}$$

$$\frac{T}{N}\sum_q \chi_{ch}(q) = \langle (n_\uparrow + n_\downarrow)^2 \rangle - n^2 = n + 2\langle n_\uparrow n_\downarrow \rangle - n^2$$

where n is the density. The above equations, in addition to [32]

$$U_{sp} = \frac{U\langle n_\uparrow n_\downarrow \rangle}{\langle n_\uparrow \rangle \langle n_\downarrow \rangle}, \tag{5}$$

suffice to determine the constant vertices U_{sp} and U_{ch}.

Once the two-particle quantities have been found as above, the next step of the approach of Ref. 22, consists in improving the approximation for the single-particle self-energy by starting from an exact expression where the high-frequency Hartree−Fock behavior is explicitly factored out. One then substitutes in the exact expression the irreducible low-frequency vertices U_{sp} and U_{ch} as well as $G_{\sigma}^{(1)}(k+q)$ and $\chi_{\text{sp}}(q), \chi_{\text{ch}}(q)$ computed above. The exact form for the self-energy expression can however be obtained either in the longitudinal or in the transverse channel. To satisfy crossing symmetry of the fully reducible vertex appearing in the general expression and to preserve consistency between one- and two-particle quantities, one averages the two possibilities to obtain [36]

$$\Sigma_{\sigma}^{(2)}(k) = U n_{-\sigma} + \frac{U}{8}\frac{T}{N}\sum_q [3 U_{\text{sp}}\chi_{\text{sp}}(q) + U_{\text{ch}}\chi_{\text{ch}}(q)] \times$$
$$\times G_{\sigma}^{(1)}(k+q). \qquad (6)$$

The resulting self-energy $\Sigma_{\sigma}^{(2)}(k)$ on the left hand-side is at the next level of approximation so it differs from the self-energy entering the right-hand side. One can verify that the longitudinal spin fluctuations contribute an amount $U\langle n_\uparrow n_\downarrow\rangle/4$ to the consistency condition [23] $(1/2)\,\text{Tr}\,(\Sigma^{(2)}G^{(1)}) = U\langle n_\uparrow n_\downarrow\rangle$ and that each of the two transverse spin components as well as the charge fluctuations also each contribute $U\langle n_\uparrow n_\downarrow\rangle/4$. In addition, one verifies numerically that the exact sum rule [22]

$$-\int d\omega'\,\text{Im}\,[\Sigma_\sigma(\mathbf{k}, \omega')]/\pi = U^2 n_{-\sigma}(1 - n_{-\sigma})$$

determining the high-frequency behavior is satisfied to a high degree of accuracy.

The theory also has a consistency check. Indeed, the exact expression for consistency between one- and two-particle quantities should be written with $G^{(2)}$ given by $(G^{-1})^{(2)} = (G^{-1})^{(0)} - \Sigma^{(2)}$ instead of with $G^{(1)}$. In other words $(1/2)\,\text{Tr}\,(\Sigma^{(2)}G^{(2)}) = U\langle n_\uparrow n_\downarrow\rangle$ should be satisfied instead of $(1/2)\,\text{Tr}\,(\Sigma^{(2)}G^{(1)}) = U\langle n_\uparrow n_\downarrow\rangle$, which is exactly satisfied here. We find through benchmarks that when the left- and right-hand side of the last equation differ only by a few percent, then the theory is accurate.

To obtain the thermodynamics, one finds the entropy by integrating $1/T$ times the specific heat $(\partial E/\partial T)$ so that we know $F = E - TS$. There are other ways to obtain the thermodynamics and one looks for consistency between these [39]. We will not discuss thermodynamic aspects in the present review.

At weak coupling in the repulsive model the particle-hole channel is the one that is influenced directly. Correlations in crossed channels, such as pairing susceptibilities, are induced indirectly and are harder to evaluate. This simply reflects the fact the simplest Hartree−Fock factorization of the Hubbard model does not lead to a d-wave order parameter (even though Hartree−Fock factorization of its strong-coupling version does). The $d_{x^2-y^2}$-wave susceptibility is defined by $\chi_d = \int_0^\beta d\tau \langle T_\tau \Delta(\tau)\Delta^\dagger\rangle$ with the d-wave order parameter equal to $\Delta^\dagger = \sum_i \sum_\gamma g(\gamma) c_{i\uparrow}^\dagger c_{i+\gamma\downarrow}^\dagger$ the sum over γ being over nearest-neighbors, with $g(\gamma) = \pm 1/2$ depending on whether γ is a neighbor along the $\hat{\mathbf{x}}$ or the $\hat{\mathbf{y}}$ axis. Briefly speaking [40,41], to extend TPSC to compute pairing susceptibility, we begin from the Schwinger−Martin−Kadanoff−Baym formalism with both diagonal [40,41] and off-diagonal [22,23] source fields. The self-energy is expressed in terms of spin and charge fluctuations and the irreducible vertex entering the Bethe−Salpeter equation for the pairing susceptibility is obtained from functional differentiation. The final expression for the d-wave susceptibility is,

$$\chi_d(\mathbf{q} = 0, iq_n = 0) = \frac{T}{N}\sum_k (g_d^2(\mathbf{k})G_\uparrow^{(2)}(-k)G_\downarrow^{(2)}(k)) -$$
$$-\frac{U}{4}\left(\frac{T}{N}\right)^2 \sum_{k,k'} g_d(\mathbf{k})G_\uparrow^{(2)}(-k)G_\downarrow^{(2)}(k) \times$$
$$\times \left(\frac{3}{1 - \frac{1}{2}U_{\text{sp}}\chi_0(k'-k)} + \frac{1}{1 + \frac{1}{2}U_{\text{ch}}\chi_0(k'-k)}\right) \times$$
$$\times G_\uparrow^{(1)}(-k')G_\downarrow^{(1)}(k')g_d(\mathbf{k'}). \qquad (7)$$

In the above expression, $g_d(\mathbf{k})$ is the form factor for the gap symmetry, while k and k' stand for both wave-vector and fermionic Matsubara frequencies on a square-lattice with N sites at temperature T. The spin and charge susceptibilities take the form $\chi_{\text{sp}}^{-1}(q) = \chi_0(q)^{-1} - 1/2\,U_{\text{sp}}$ and $\chi_{\text{ch}}^{-1}(q) = \chi_0(q)^{-1} + 1/2 U_{\text{ch}}$ with χ_0 computed with the Green function $G_\sigma^{(1)}$ that contains the self-energy whose functional differentiation gave the spin and charge vertices. The values of U_{sp}, U_{ch} and $\langle n_\uparrow n_\downarrow\rangle$ are obtained as described above. In the pseudogap regime, one cannot use $U_{\text{sp}} = U\langle n_\uparrow n_\downarrow\rangle/(\langle n_\uparrow\rangle\langle n_\downarrow\rangle)$. Instead [22], one uses the local-moment sum rule with the zero temperature value of $\langle n_\uparrow n_\downarrow\rangle$ obtained by the method of Ref. 42 that agrees very well with QMC calculations at all

values of U. Also, $G_\sigma^{(2)}$ contains self-energy effects coming from spin and charge fluctuations, as described above [34,36].

The same principles and methodology can be applied for the attractive Hubbard model [40,43,44]. In that case, the dominant channel is the s-wave pairing channel. Correlations in the crossed channel, namely the spin and charge susceptibilities, can also be obtained *mutatis mutandi* along the lines of the previous paragraph.

2.1.2. Benchmarks for TPSC

To test any non-perturbative approach, we need reliable benchmarks. Quantum Monte Carlo (QMC) simulations provide such benchmarks. The results of such numerical calculations are unbiased and they can be obtained on much larger system sizes than any other simulation method. The statistical uncertainty can be made as small as required. The drawback of QMC is that the sign problem renders calculations impossible at temperatures low enough to reach those that are relevant for d-wave superconductivity. Nevertheless, QMC can be performed in regimes that are non-trivial enough to allow us to eliminate some theories on the grounds that they give qualitatively incorrect results. Comparisons with QMC allow us to estimate the accuracy of the theory. An approach like TPSC can then be extended to regimes where QMC is unavailable with the confidence provided by agreement between both approaches in regimes where both can be performed.
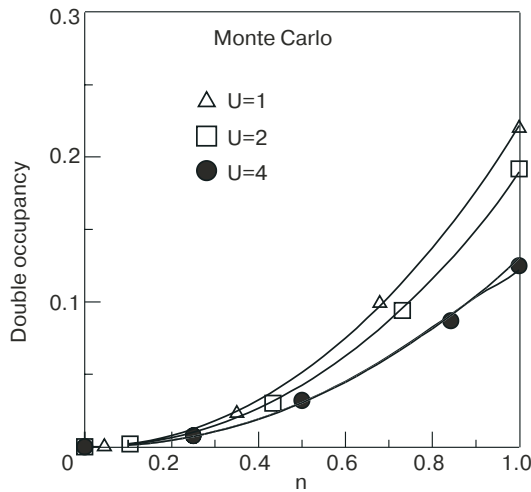

Fig. 2. Comparisons between the QMC simulations (symbols) and TPSC (solid lines) for the filling dependence of the double occupancy. The results are for $T = t/6$ as a function of filling and for various values of U expect for $U = 4t$ where the dashed line shows the results of our theory at the crossover temperature $T = T_X$. From Ref. 22.
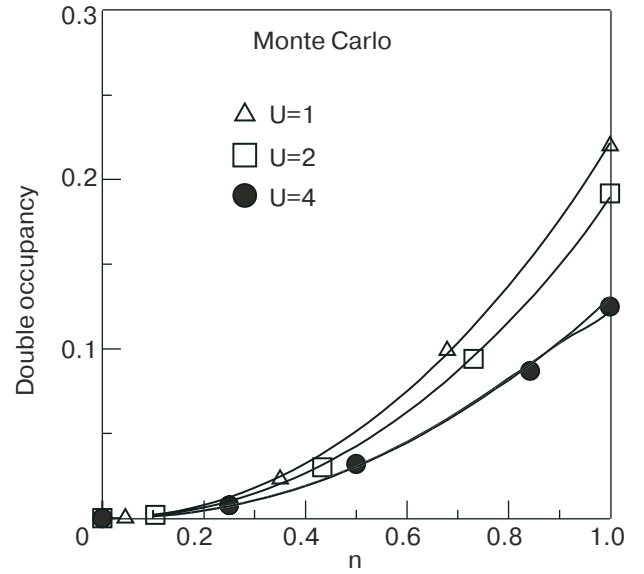

Fig. 3. Wave vector $\mathbf{q}$ dependence of the spin and charge structure factors for different sets of parameters. Solid lines are from TPSC and symbols are our QMC data. Monte Carlo data for $n = 1$ and $U = 8t$ are for 6×6 clusters and $T = 0.5t$; all other data are for 8×8 clusters and $T = 0.2t$. Error bars are shown only when significant. From Ref. 32.

In order to be concise, details are left to figure captions. Let us first focus on quantities related to spin and charge fluctuations. The symbols on the figures refer to QMC results while the solid lines come from TPSC calculations. Fig. 2 shows double occupancy, a quantity that plays a very important role in the Hubbard model in general and in TPSC in particular. That quantity is shown as a function of filling for various values of U at inverse temperature $\beta = 6$. Figure 3 displays the spin and charge structure factors in a regime where size effects are not important. Clearly the results are non-perturbative given the large difference between the spin and charge structure factors, which are plotted here in units where they are equal at $U = 0$. In Fig. 4 we exhibit the static structure factor at half-filling as a function of temperature. Below the crossover temperature T_X, there is an important size dependence in the QMC results. The TPSC calculation, represented by a solid line, is done for an infinite system. We see that the mean-field finite transition temperature T_{MF} is replaced by a crossover temperature T_X at which the correlations enter an exponential growth regime. One can show analytically [22,32] that the correlation length becomes infinite only at zero temperature, thus satisfying the Mermin−Wagner theorem. The QMC results approach the TPSC results as the system size grows. Nevertheless, TPSC is in the $N = \infty$ universality class [45] contrary to the Hubbard model for which $N = 3$, so one expects quantitative differences
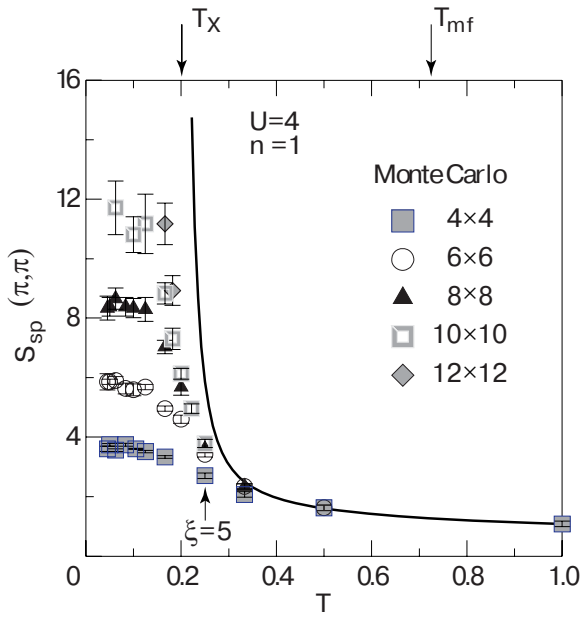
Fig. 4. Temperature dependence of $S_{sp}(\pi,\pi)$ at half-filling $n = 1$. The solid line is from TPSC and symbols are Monte Carlo data from Ref. 46. Taken from Ref. 32.

to increase as the correlation length becomes larger. It is important to note that T_X does not coincide with the mean-field transition temperature T_{MF}. This is because of Kanamori−Brueckner screening [32,47] that manifests itself in the difference between U_{sp} and the bare U. Below T_X, the main contribution to the static spin structure factor in Fig. 4 comes from the zero-Matsubara frequency component of the spin susceptibility. This is the so-called renormalized classical regime where the characteristic spin fluctuation frequency ω_{sp} is much less than temperature. Even at
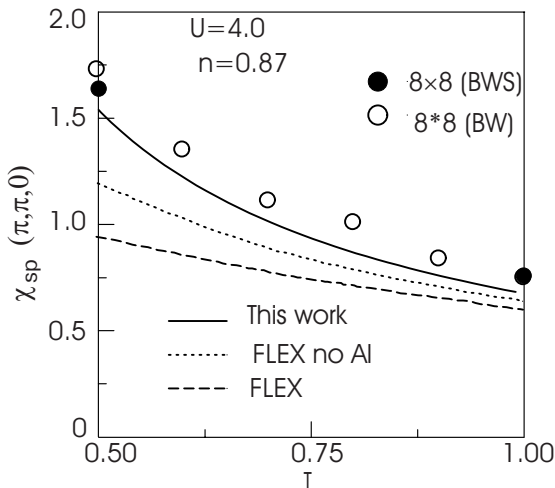

Fig. 5. Comparisons between Monte Carlo simulations (BW), FLEX calculations and TPSC for the spin susceptibility at $Q = (\pi,\pi)$ as a function of temperature at zero Matsubara frequency. The filled circles (BWS) are from Ref. 48. Taken from Ref. 22.
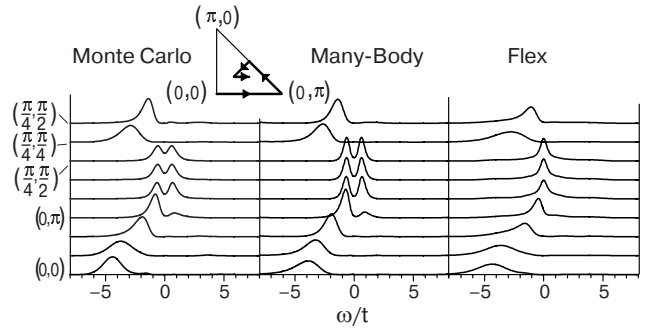

Fig. 6. Single particle spectral weight $A(\mathbf{k},\omega)$ for $U = 4t$, $\beta = 5/t$, $n = 1$, and all independent wave vectors $\mathbf{k}$ of an 8×8 lattice. Results obtained from maximum entropy inversion of QMC data on the left panel and many-body TPSC calculations with Eq. (6) on the middle panel and with FLEX on the right panel. From Ref. 36.

temperatures higher than that, TPSC agrees with QMC calculation much better than other methods, as shown in Fig. 5.

Below the crossover temperature to the renormalized classical regime, a pseudogap develops in the single-particle spectral weight. This is illustrated in Fig. 6 [36]. Eliashberg-type approaches such as FLEX do not show the pseudogap present in QMC. The size dependence of the results is also quite close in TPSC and in QMC, as shown in Fig. 7.

The *d*-wave susceptibility [41] shown in Fig. 8 again clearly demonstrates the agreement between TPSC and QMC. In particular, the dome shape dependence of the QMC results is reproduced to within a few percent. We will see in Sec. 3 how one understands the dome shape and the fact that the *d*-wave susceptibility of the interacting system is smaller than that of the non-interacting one in this temperature range.
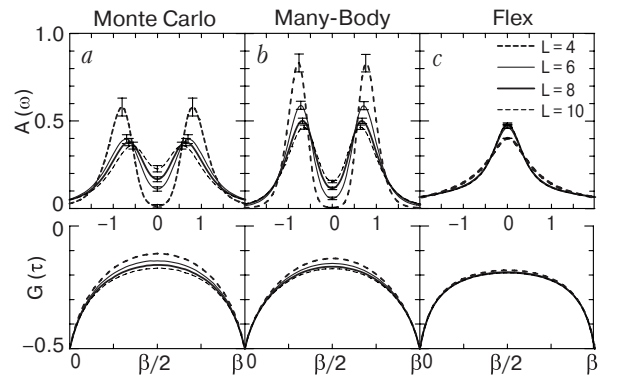

Fig. 7. Size dependent results for various types of calculations for $U = 4t$, $\beta = 5/t$, $n = 1$, $\mathbf{k} = (0,\pi)$, $L = 4, 6, 8, 10$. Upper panels show $A(\mathbf{k},\omega)$ extracted from maximum entropy on $G(\tau)$ shown on the corresponding lower panels. QMC (*a*), TPSC using Eq. (6) (*b*), FLEX (*c*). From Ref. 36.
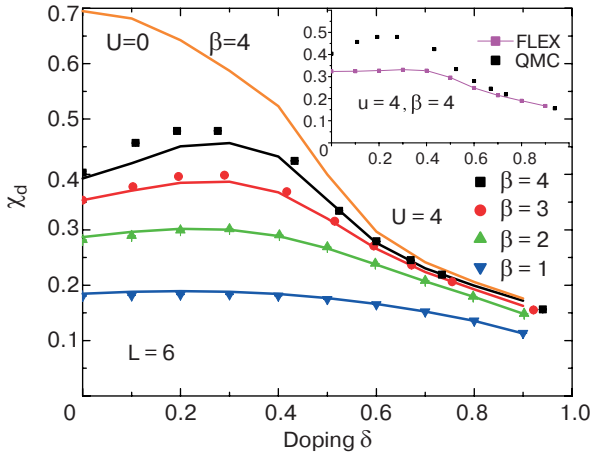
Fig. 8. Comparisons between the $d_{x^2-y^2}$ susceptibility obtained from QMC simulations (symbols) and from the TPSC approach (lines) in the two-dimensional Hubbard model. Both calculations are for $U = 4t$, a 6×6 lattice. QMC error bars are smaller than the symbols. Analytical results are joined by solid lines. The size dependence of the results is small at these temperatures. The $U = 0$ case is also shown at $\beta = 4/t$ as the upper line. The inset compares QMC and FLEX at $U = 4, \beta = 4/t$. From Ref. 41.

To conclude this section, we quickly mention a few other results obtained with TPSC. Fig. 9 contrasts the crossover phase diagram obtained for the Hubbard model at the van Hove filling [49] with the results of a renormalization group calculation [27]. The difference occurring in the ferromagnetic region is
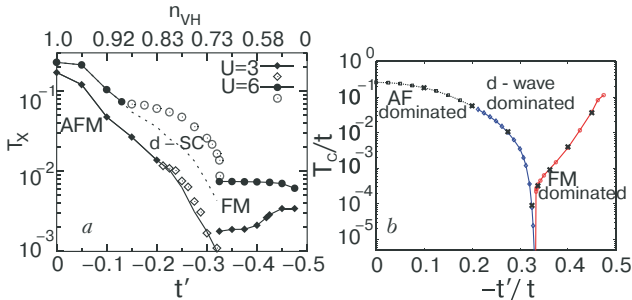

Fig. 9. The crossover diagram as a function of next-nearest-neighbor hopping t' from TPSC (*a*) and from a temperature cutoff renormalization group technique from Ref. 27 (*b*). The corresponding Van Hove filling is indicated on the upper horizontal axis. Crossover lines for magnetic instabilities near the antiferromagnetic and ferromagnetic wave vectors are represented by filled symbols while open symbols indicate instability towards $d_{x^2-y^2}$-wave superconducting. The solid and dashed lines below the empty symbols show, respectively for $U = 3t$ and $U = 6t$, where the antiferromagnetic crossover temperature would have been in the absence of the superconducting instability. The largest system size used for this calculation is 2048×2048. From Ref. 49.
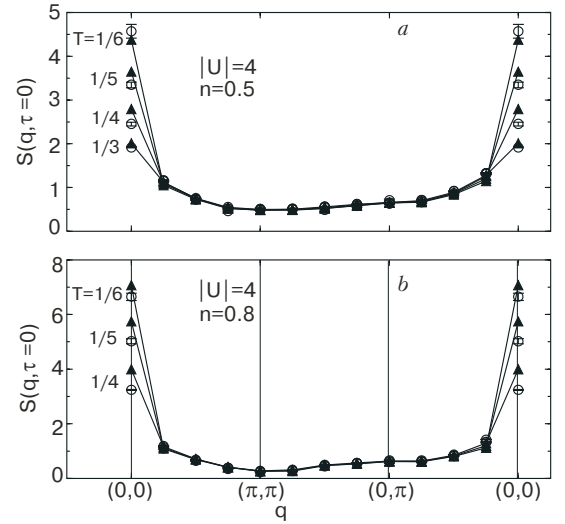

Fig. 10. TPSC *s*-wave paring structure factor $S(\mathbf{q}, \tau = 0)$ (filled triangles) and QMC $S(\mathbf{q}, \tau = 0)$ (open circles) for $U = -4t$ and various temperatures (*a*) at $n = 0.5$ and (*b*) at $n = 0.8$ on a 8×8 lattice. The dashed lines are to guide the eye. From Ref. 44.

discussed in detail in Ref. 49. Finally, we point out various comparisons for the attractive Hubbard model. Fig. 10 shows the static *s*-wave pairing susceptibility, Fig. 11 the chemical potential and the occupation number, and finally Fig. 12 the local density of states and the single-particle spectral weight at a given wave vector.

2.2. Strong-coupling approaches: quantum clusters

DMFT [3,50] has been extremely successful in helping us understand the Mott transition, the key physical phenomenon that manifests itself at strong coupling. However, in high dimension where this
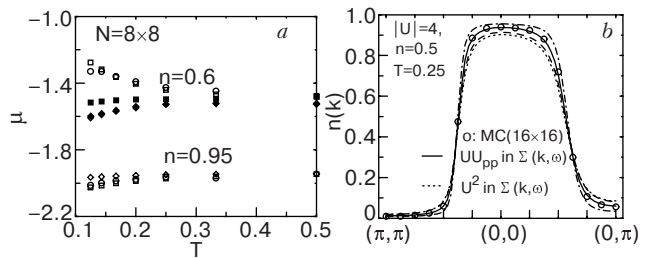

Fig. 11. Chemical potential shifts $\mu^{(1)} - \mu_0$ (open diamonds) and $\mu^{(2)} - \mu_0$ (open squares) with the results of QMC calculations (open circles) for $U = -4t$ (*a*). The momentum dependent occupation number $n(\mathbf{k})$. Circles: QMC calculations from Ref. 51. The solid curve: TPSC. The dashed curve obtained by replacing U_{pp} by U in the self-energy with all the rest unchanged. The long-dash line is the result of a self-consistent T-matrix calculation, and the dot-dash line the result of second-order perturbation theory (*b*). From Ref. 44.
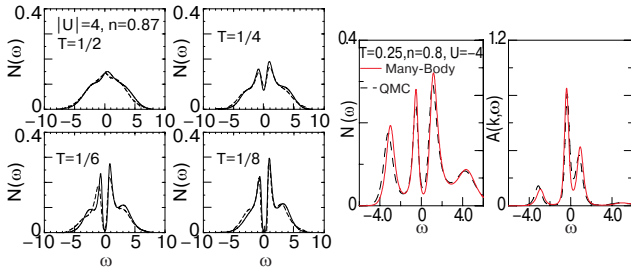
Fig. 12. Comparisons of local density of states and single-particle spectral weight from TPSC (solid lines) and QMC (dashed lines) on a 8×8 lattice. QMC data for the density of states taken from Ref. 52 ($t = 1/4$). Figures from Ref. 44.

theory becomes exact, spatial fluctuations associated with incipient order do not manifest themselves in the self-energy. In low dimension, this is not the case. The self-energy has strong momentum dependence, as clearly shown experimentally in the high-temperature superconductors, and theoretically in the TPSC approach, a subject we shall discuss again below. It is thus necessary to go beyond DMFT by studying clusters instead of a single Anderson impurity as done in DMFT. The simplest cluster approach that includes strong-coupling effects and momentum dependence is CPT [55,54]. In this approach, an infinite set of disconnected clusters are solved exactly and then connected to each other using strong-coupling perturbation theory. Although the resulting theory turns out to give the exact result in the $U = 0$ case, its derivation clearly shows that one expects reliable results mostly at strong coupling. This approach does not include the self-consistent effects contained in DMFT. Self-consistency was first included within DCA [55], where a momentum-space cluster is connected to a self-consistent momentum-space medium. In our opinion, the best framework to understand all other cluster methods is the self-energy functional approach of Potthoff [56,57]. The form of the lattice Green function obtained in this approach is the same as that obtained in CPT, clearly exhibiting that such an approach is better at strong-coupling, even though results often extrapolate correctly to weak coupling. Amongst the special cases of this approach, the VCA, or VCPT [57] is the one closest to the original approach. In a variant, CDMFT [58], a cluster is embedded in a self-consistent medium instead of a single Anderson impurity as in DMFT. The strong-coupling aspects of CDMFT come out clearly in Refs. 59,60. A detailed review of quantum cluster methods has appeared in Ref. 61.

2.2.1. Cluster perturbation theory

Even though CPT does not have the self-consistency present in DMFT type approaches, at fixed computing resources it allows for the best momentum resolution. This is particularly important for the ARPES pseudogap in electron-doped cuprates that has quite a detailed momentum space structure, and for d-wave superconducting *co*rrelations where the zero temperature pair correlation length may extend well beyond near-neighbor sites. CPT was developed by Gros [53] and Sénéchal [54] independently. This approach can be viewed as the first term of a systematic expansion around strong coupling [62]. Let us write the hopping matrix elements in the form

$$t_{\mu\nu}^{mn} = t_{\mu\nu}^{(c)} \delta_{mn} + V_{\mu\nu}^{mn} \qquad (8)$$

where m and n label the different clusters, and μ, ν label the sites within a cluster. Then $t_{\mu\nu}^{(c)}$ labels all the hopping matrix elements within a cluster and the above equation defines $V_{\mu\nu}^{mn}$.

We pause to introduce the notation that will be used throughout for quantum cluster methods. We follow the review article Ref. 61. In reciprocal space, any wave vector $\mathbf{k}$ in the Brillouin zone may be written as $\mathbf{k} = \tilde{\mathbf{k}} + \mathbf{K}$ where both $\mathbf{k}$ and $\tilde{\mathbf{k}}$ are continuous in the infinite size limit, except that $\tilde{\mathbf{k}}$ is defined only in the reduced Brillouin zone that corresponds to the superlattice. On the other hand, $\mathbf{K}$ is discrete and denotes reciprocal lattice vectors of the superlattice. By analogy, any position $\mathbf{r}$ in position space can be written as $\tilde{\mathbf{r}} + \mathbf{R}$ where $\mathbf{R}$ is for positions within clusters while $\tilde{\mathbf{r}}$ labels the origins of the clusters, an infinite number of them. Hence, Fourier's theorem allows one to define functions of $\mathbf{k}, \tilde{\mathbf{k}}$ or $\mathbf{K}$ that contain the same information as functions of, respectively, $\mathbf{r}, \tilde{\mathbf{r}}$ or $\mathbf{R}$. Also, we have $\mathbf{K} \cdot \tilde{\mathbf{r}} = 2\pi n$ where n is an integer. Sites within a cluster are labelled by greek letters so that the position of site μ within a cluster is $\mathbf{R}_\mu$, while clusters are labelled by Latin letters so that the origin of cluster m is at $\tilde{\mathbf{r}}_m$.

Returning to CPT, the Green function for the whole system is given by

$$[\hat{G}^{-1}(\tilde{\mathbf{k}}, z)]_{\mu\nu} = [\hat{G}^{(c)-1}(z) - \hat{V}(\tilde{\mathbf{k}})]_{\mu\nu} \qquad (9)$$

where hats denote matrices in cluster site indices and z is the complex frequency. At this level of approximation, the CPT Green function has the same structure as in the Hubbard I approximation except that it pertains to a cluster instead of a single site. Since $\hat{G}^{(c)-1}(z) = z + \mu - \hat{t}^{(c)} - \hat{\Sigma}^{(c)}$ and $\hat{G}^{(0)-1}(\tilde{\mathbf{k}}, z) = z + \mu - \hat{t}^{(c)} - \hat{V}(\tilde{\mathbf{k}})$, the Green function (9) may also be written as

$$\hat{G}^{-1}(\tilde{\mathbf{k}}, z) = \hat{G}^{(0)-1}(\tilde{\mathbf{k}}, z) - \hat{\Sigma}^{(c)}(z). \qquad (10)$$

This form allows a different physical interpretation of the approach. In the above expression, the self-energy of the lattice is approximated by the self-energy of the cluster. The latter in real space spans only the size of the cluster.

We still need an expression to extend the above result to the lattice in a translationally invariant way. This is done by defining the following residual Fourier transform:

$$G_{CPT}(\mathbf{k}, z) = \frac{1}{N_c} \sum_{\mu,\nu}^{N_c} e^{i\mathbf{k}\cdot(\mathbf{R}_\mu - \mathbf{R}_\nu)} G_{\mu\nu}(\tilde{\mathbf{k}}, z). \quad (11)$$

Notice that $G_{\mu\nu}(\tilde{\mathbf{k}}, z)$ may be replaced by $G_{\mu\nu}(\mathbf{k}, z)$ in the above equation since $\hat{V}(\mathbf{k} + \mathbf{K}) = \hat{V}(\tilde{\mathbf{k}})$.

2.2.2. Self-energy functional approach

The self-energy functional approach, devised by Potthoff [57] allows one to consider various cluster schemes from a unified point of view. It begins with $\Omega_{\mathbf{t}}[G]$, a functional of the Green function

$$\Omega_{\mathbf{t}}|G| = \Phi|G| - \text{Tr}\,[(G_{0\mathbf{t}}^{-1} - G^{-1})\,G] + \text{Tr}\,\ln\,(-G). \qquad (12)$$

The Luttinger–Ward functional $\Phi|G|$ entering this equation is the sum of connected vacuum skeleton diagrams. A diagram-free definition of this functional is also given in Ref. 63. For our purposes, what is important is that (1) The functional derivative of $\Phi[G]$ is the self-energy

$$\frac{\delta\Phi|G|}{\delta G} = \Sigma \qquad (13)$$

and (2) it is a universal functional of G in the following sense: whatever the form of the one-body Hamiltonian, it depends only on the interaction and, functionnally, it has the same dependence on G. The dependence of the functional $\Omega_{\mathbf{t}}|G|$ on the one-body part of the Hamiltonian is denoted by the subscript $\mathbf{t}$ and it comes only through $G_{0\mathbf{t}}^{-1}$ appearing on the right-hand side of Eq. (12).

The functional $\Omega_{\mathbf{t}}|G|$ has the important property that it is stationary when G takes the value prescribed by Dyson's equation. Indeed, given the last two equations, the Euler equation takes the form

$$\frac{\delta\Omega_{\mathbf{t}}|G|}{\delta G} = \Sigma - G_{0\mathbf{t}}^{-1} + G^{-1} = 0. \qquad (14)$$

This is a dynamic variational principle since it involves the frequency appearing in the Green function, in other words excited states are involved in the variation. At this stationary point, and only there,

$\Omega_{\mathbf{t}}|G|$ is equal to the grand potential. Contrary to Ritz's variational principle, this last equation does not tell us whether $\Omega_{\mathbf{t}}|G|$ is a minimum or a maximum or a saddle point there.

There are various ways to use the stationarity property that we described above. The most common one, is to approximate $\Phi|G|$ by a finite set of diagrams. This is how one obtains the Hartree–Fock, the FLEX approximation [21] or other so-called thermodynamically consistent theories. This is what Potthoff calls a type II approximation strategy [64]. A type I approximation simplifies the Euler equation itself. In a type III approximation, one uses the exact form of $\Phi|G|$ but only on a limited domain of trial Green functions.

Following Potthoff, we adopt the type III approximation on a functional of the self-energy instead of on a functional of the Green function. Suppose we can locally invert Eq. (13) for the self-energy to write G as a functional of Σ. We can use this result to write,

$$\Omega_{\mathbf{t}}|\Sigma| = F|\Sigma| - \text{Tr}\,\ln\,(-G_{0\mathbf{t}}^{-1} + \Sigma), \qquad (15)$$

where we defined

$$F|\Sigma| = \Phi|G| - \text{Tr}\,(\Sigma G). \qquad (16)$$

and where it is implicit that $G = G[\Sigma]$ is now a functional of Σ. $F[\Sigma]$, along with the expression (13) for the derivative of the Luttinger–Ward functional, define the Legendre transform of the Luttinger–Ward functional. It is easy to verify that

$$\frac{\delta F|\Sigma|}{\delta\Sigma} = \frac{\delta\Phi|G|}{\delta G}\frac{\delta G|\Sigma|}{\delta\Sigma} - \Sigma\frac{\delta G|\Sigma|}{\delta\Sigma} - G = -G \quad (17)$$

hence, $\Omega_{\mathbf{t}}|\Sigma|$ is stationary with respect to Σ when Dyson's equation is satisfied

$$\frac{\delta\Omega_{\mathbf{t}}|\Sigma|}{\delta\Sigma} = -G + (G_{0\mathbf{t}}^{-1} - \Sigma)^{-1} = 0. \qquad (18)$$

To perform a type III approximation on $F[\Sigma]$, we take advantage that it is universal, i.e., that it depends only on the interaction part of the Hamiltonian and not on the one-body part. This follows from the universal character of its Legendre transform $\Phi|G|$. We thus evaluate $F|\Sigma|$ exactly for a Hamiltonian H' that shares the same interaction part as the Hubbard Hamiltonian, but that is exactly solvable. This Hamiltonian H' is taken as a cluster decomposition of the original problem, i.e., we tile the infinite lattice into identical, disconnected clusters that can be solved exactly. Examples of such tilings are given in Fig. 13. Denoting the corresponding quantities with a prime, we obtain,

$$\Omega_{\mathbf{t}'}|\Sigma'| = F|\Sigma'| - \text{Tr}\,\ln\,(-G_{0\mathbf{t}'}^{-1} + \Sigma'), \qquad (19)$$
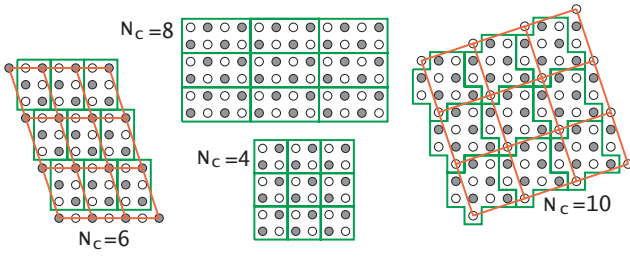
Fig. 13. Various tilings used in quantum cluster approaches. In these examples the grey and white sites are inequivalent since an antiferromagnetic order is possible.

from which we can extract $F[\Sigma']$. It follows that

$$\Omega_{\mathbf{t}}[\Sigma'] = \Omega_{\mathbf{t}'}[\Sigma'] + \mathrm{Tr}\,\ln\,(-G_{0\mathbf{t}'}^{-1} + \Sigma') -$$
$$- \mathrm{Tr}\,\ln\,(-G_{0\mathbf{t}}^{-1} + \Sigma'). \quad (20)$$

The type III approximation comes from the fact that the self-energy Σ' is restricted to the exact self-energy of the cluster problem H', so that variational parameters appear in the definition of the one-body part of H'.

In practice, we look for values of the cluster one-body parameters $\mathbf{t}'$ such that $\delta\Omega_{\mathbf{t}}[\Sigma']/\delta\mathbf{t}' = 0$. It is useful for what follows to write the latter equation formally, although we do not use it in actual calculations. Given that $\Omega_{\mathbf{t}'}[\Sigma']$ is the actual grand potential evaluated for the cluster, $\partial\Omega_{\mathbf{t}'}[\Sigma']/\partial\mathbf{t}'$ is canceled by the explicit $\mathbf{t}'$ dependence of $\mathrm{Tr}\,\ln\,(-G_{0\mathbf{t}'}^{-1} + \Sigma')$ and we are left with

$$0 = \frac{\delta\Omega_{\mathbf{t}}[\Sigma']}{\delta\Sigma'}\frac{\delta\Sigma'}{\delta\mathbf{t}'} = -\mathrm{Tr}\left[\left(\frac{1}{G_{0\mathbf{t}'}^{-1} - \Sigma'} - \frac{1}{G_{0\mathbf{t}}^{-1} - \Sigma'}\right)\frac{\delta\Sigma'}{\delta\mathbf{t}'}\right]. \quad (21)$$

Given that the clusters corresponding to $\mathbf{t}'$ are disconnected and that translation symmetry holds on the superlattice of clusters, each of which contains N_c sites, the last equation may be written

$$\sum_{\omega_n}\sum_{\mu\nu}\left[\frac{N}{N_c}\left(\frac{1}{G_{0\mathbf{t}'}^{-1} - \Sigma'(i\omega_n)}\right)_{\mu\nu} - \right.$$
$$\left. - \sum_{\tilde{\mathbf{k}}}\left(\frac{1}{G_{0\mathbf{t}}^{-1}(\tilde{\mathbf{k}}) - \Sigma'(i\omega_n)}\right)_{\mu\nu}\right] \times \frac{\delta\Sigma'_{\nu\mu}(i\omega_n)}{\delta\mathbf{t}'} = 0. \quad (22)$$

2.2.3. Variational cluster perturbation theory, or variational cluster approximation

In VCPT, more aptly named the Variational Cluster Approach (VCA), solutions to the Euler equations (22) are found by looking for numerical minima (or more generally, saddle-points) of the functional. Typically, the VCA cluster Hamiltonian H' will have

the same form as H except that there is no hopping between clusters and that long-range order is allowed by adding some Weiss fields, for instance like in Eq. (36) below. The hopping terms and chemical potential within H' may also be treated like additional variational parameters. In contrast with mean-field theory, these Weiss fields are not mean fields, in the sense that they do not coincide with the corresponding order parameters. The interaction part of H (or H') is not factorized in any way and short-range correlations are treated exactly. In fact, the Hamiltonian H is not altered in any way; the Weiss fields are introduced to let the variational principle act on a space of self-energies that includes the possibility of specific long-range orders, without imposing those orders. Indeed, the more naturally an order arises in the system, the smaller the Weiss field needs to be, and one observes that the strength of the Weiss field at the stationary point of the self-energy functional generally decreases with increasing cluster size, as it should since in the thermodynamic limit no Weiss field should be necessary to establish order.

2.2.4. Cellular dynamical mean-field theory

The CDMFT is obtained by including in the cluster Hamiltonian H' a bath of uncorrelated electrons that somehow must mimic the effect on the cluster of the rest of the lattice. Explicitly, H' takes the form

$$H' = -\sum_{\mu,\nu,\sigma}t_{\mu\nu}'c_{\mu\sigma}^\dagger c_{\nu\sigma} + U\sum_\mu n_{\mu\uparrow}n_{\mu\downarrow} +$$
$$+ \sum_{\mu,\alpha,\sigma}V_{\mu\alpha}(c_{\mu\sigma}^\dagger a_{\alpha\sigma} + \mathrm{h.c.}) + \sum_\alpha \varepsilon_\alpha a_{\alpha\sigma}^\dagger a_{\alpha\sigma} \quad (23)$$

where $a_{\alpha\sigma}$ annihilates an electron of spin σ on a bath orbital labelled α. The bath is characterized by the energy of each orbital (ε_α) and the bath-cluster hybridization matrix $V_{\mu\alpha}$. This representation of the environment through an Anderson impurity model was introduced in Ref. 65 in the context of DMFT (i.e., a single site). The effect of the bath on the electron Green function is encapsulated in the so-called hybridization function

$$\Gamma_{\mu\nu}(\omega) = \sum_\alpha \frac{V_{\mu\alpha}V_{\nu\alpha}^*}{\omega - \varepsilon_\alpha} \quad (24)$$

which enters the Green function as

$$\left|G'^{-1}\right|_{\mu\nu} = \omega + \mu - t_{\mu\nu}' - \Gamma_{\mu\nu}(\omega) - \Sigma_{\mu\nu}(\omega). \quad (25)$$

Moreover, the CDMFT does not look for a strict solution of the Euler equation (22), but tries instead to set each of the terms between brackets to zero separately. Since the Euler equation (22) can be seen as a scalar product, CDMFT requires that the modulus of

one of the vectors vanish to make the scalar product vanish. From a heuristic point of view, it is as if each component of the Green function in the cluster were equal to the corresponding component deduced from the lattice Green function. This clearly reduces to single site DMFT when there is only one lattice site.

When the bath is discretized, i.e., is made of a finite number of bath «orbitals», the left-hand side of Eq. (22) cannot vanish separately for each frequency, since the number of degrees of freedom in the bath is insufficient. Instead, one adopts the following self-consistent scheme: (1) one starts with a guess value of the bath parameters $(V_{\mu\alpha}, \varepsilon_\alpha)$ and solves the cluster Hamiltonian H' numerically. (2) One then calculates the combination

$$\hat{\mathcal{G}}_0^{-1} = \left[\sum_{\tilde{\mathbf{k}}} \frac{1}{\hat{G}_{0\mathbf{t}}^{-1}(\tilde{\mathbf{k}}) - \hat{\Sigma}'(i\omega_n)}\right]^{-1} + \hat{\Sigma}'(i\omega_n) \quad (26)$$

and (3) minimizes the following canonically invariant distance function:

$$d = \sum_{n,\mu,\nu} \left|\left(i\omega_n + \mu - \hat{t}' - \hat{\Gamma}(i\omega_n) - \hat{\mathcal{G}}_0^{-1}\right)_{\mu\nu}\right|^2 \quad (27)$$

over the set of bath parameters (changing the bath parameters at this step does not require a new solution of the Hamiltonian H', but merely a recalculation of the hybridization function $\hat{\Gamma}$). The bath parameters obtained from this minimization are then put back into step (1) and the procedure is iterated until convergence.

In practice, the distance function (27) can take various forms, for instance by adding a frequency-dependent weight in order to emphasize low-frequency properties [16,59,66] or by using a sharp frequency cutoff [67]. These weighting factors can be considered as rough approximations for the missing factor $\delta\Sigma_{\nu\mu}'(i\omega_n)/\delta\mathbf{t}'$ in the Euler equation (22). The frequencies are summed over on a discrete, regular grid along the imaginary axis, defined by some fictitious inverse temperature β, typically of the order of 20 or 40 (in units of t^{-1}). Even when the total number of cluster plus bath sites in CDMFT equals the number of sites in a VCA calculation, CDMFT is much faster than the VCA since the minimization of a grand potential functional requires many exact diagonalizations of the cluster Hamiltonian H'.

The final lattice Green function from which one computes observable quantities may be obtained by periodizing the self-energy, as in Ref. 58 or in the CPT manner described above in Eq. (11). We prefer the last approach because it corresponds to the Green

function needed to obtain the density from $\partial\Omega/\partial\mu = -\text{Tr}(G)$ and also because periodization of the self-energy gives additional unphysical states in the Mott gap [68] (see also Ref. 60).

2.2.5. The Dynamical cluster approximation

The DCA [53] cannot be formulated within the self-energy functional approach*. It is based on the idea of discretizing irreducible quantities, such as the energy, in reciprocal space. It is believed to converge faster for $\mathbf{q} = 0$ quantities whereas CDMFT converges exponentially fast for local quantities [69–71].

2.2.6. Benchmarks for quantum cluster approaches

Since DMFT becomes exact in infinite dimension, the most difficult challenge for cluster extensions of
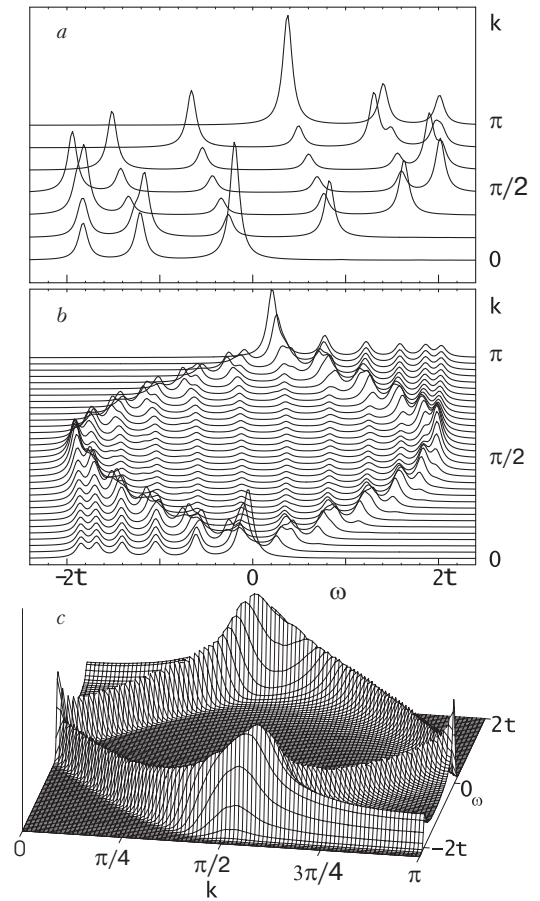

Fig. 14. The spectral function of the U limit of the one-dimensional Hubbard model, as calculated from (*a*) an exact diagonalization of the Hubbard model with $U/t = 100$ on a periodic 12-site cluster; (*b*) the same, but with CPT, on a 12-site cluster with open boundary conditions; (*c*) the exact solution, taken from Ref. 72; beware: the axes are oriented differently. In (*a*) and (*b*) a finite width η has been given to peaks that would otherwise be Dirac δ-functions.

---

* Th. Maier, M. Potthoff, and D. Sénéchal, *unpublished*.
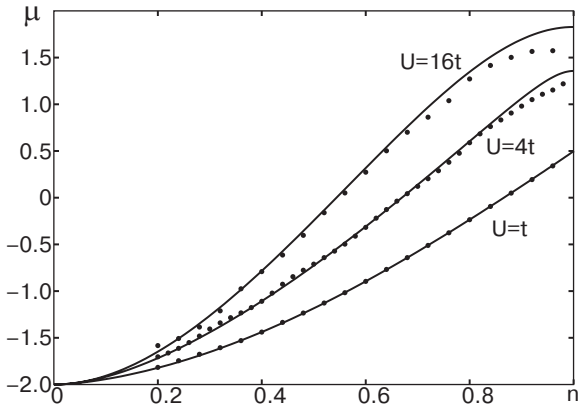
Fig. 15. Chemical potential as a function of density in the one-dimensional Hubbard model, as calculated by CPT (from Ref. 62). The exact, Bethe−Ansatz result is shown as a solid line.
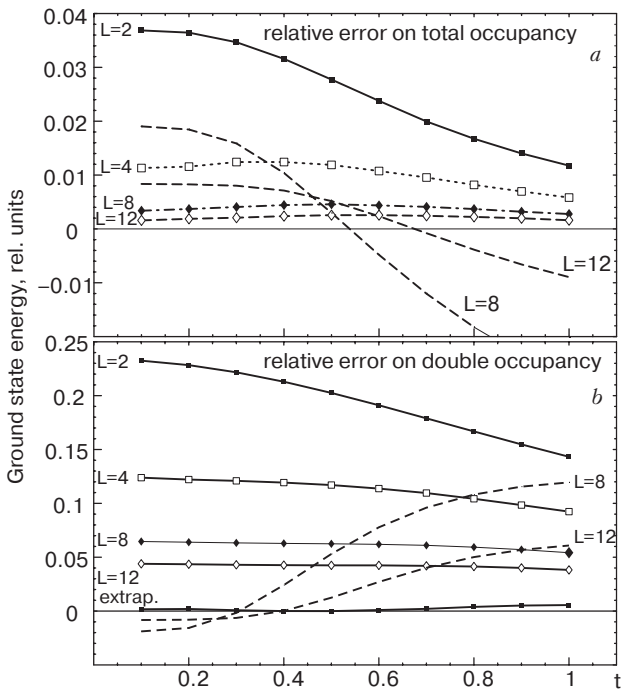

Fig. 16. Comparison (expressed in relative difference) between the ground-state energy density of the half-filled, one-dimensional Hubbard model calculated from the exact, Bethe−Ansatz result. The results are displayed as a function of the hopping t, for $U = 2t$ and various cluster sizes L (connected symbols). For comparison, the exact diagonalization values of finite clusters with periodic boundary conditions are also shown (dashed lines) for $L = 8$ and $L = 12$ (*a*). Bottom: Same for the double occupancy. An extrapolation of the results to infinite cluster size ($L \rightarrow \infty$) using a quadratic fit in terms of $1/L$ is also shown, and is accurate to within 0.5% (*b*). Taken from Ref. 62.

this approach is in one dimension. In addition, exact results to compare with exist only in one dimension so it is mostly in $d = 1$ that cluster methods have been checked. In $d = 2$ there have also been a few comparisons with QMC as we shall discuss.

CPT has been checked [68] for example by comparing with exact results [72] for the spectral function at $U \rightarrow \infty$ in $d = 1$ as shown in Fig. 14. Figure 15 shows the chemical potential as a function of density for various values of U. Figure 16 shows the convergence rates for the total energy and for the double occupancy in the $d = 1$ half-filled model. Clearly, there is a dramatic improvement compared with exact diagonalizations.

The main weakness of CPT is that it cannot take into account tendency towards long-range order. This is remedied by VCPT, as shown in Fig. 17 where CPT, VCPT are both compared with QMC as a benchmark. Despite this agreement, we should stress that long wave length fluctuations are clearly absent from cluster approaches. Hence, the antiferromagnetic order parameter at half-filling, for example, does not contain the effect of zero-point long wave length transverse spin fluctuations. This is discussed for example in the context of Fig. 9 of Ref. 73.

CDMFT corrects the difficulties of CPT near half-filling by reproducing the infinite compressibility predicted by the Bethe ansatz in one dimension as shown in Fig. 18 [74]. Detailed comparisons between the local and near-neighbor Green functions [66,74] have
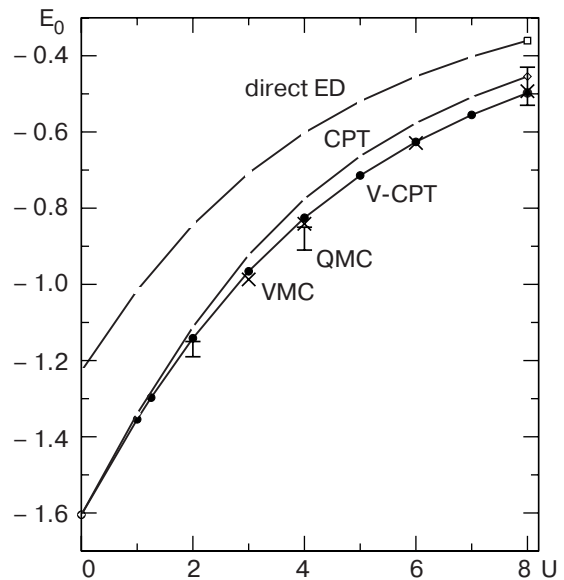

Fig. 17. Ground state energy of the half-filled, two-dimensional Hubbard model ($t = 1$) as a function of U, as obtained from various methods: exact diagonalization (ED), CPT and VCPT on a 10-site cluster, quantum Monte Carlo (QMC) and variational Monte Carlo (VMC). Taken from Ref. 73.

been performed. One should note that these results, obtained from exact diagonalization, also need the definition of a distance function (See Eq. (27) above) that helps find the best bath parametrization to satisfy the self-consistency condition. This measure forces one to define calculational parameters such as a frequency cutoff and an fictitious temperature defining the Matsubara frequencies to sum over. The final results are not completely insensitive to the choice of fictitious temperature or frequency-weighing scheme but are usually considered reliable and consistent with each other when β lies between 20 and 40. The cutoff procedures have been discussed in Ref. 67.

The relative merits of DCA and CDMFT have been discussed for example in Refs. 69–71,75,76. Briefly speaking, convergence seems faster in DCA for long wave length quantities but CDMFT is faster (exponentially) for local quantities.

3. Results and concordance between different methods

In this section, we outline the main results we obtained concerning the pseudogap and d-wave superconductivity in the two-dimensional Hubbard model. Quantum cluster approaches are better at strong coupling while TPSC is best at weak coupling. Nevertheless, all these methods are non-perturbative, the intermediate coupling regime presenting the physically most interesting case. But it is also the regime where we have the least control over the approximations. As we will show, it is quite satisfying that,
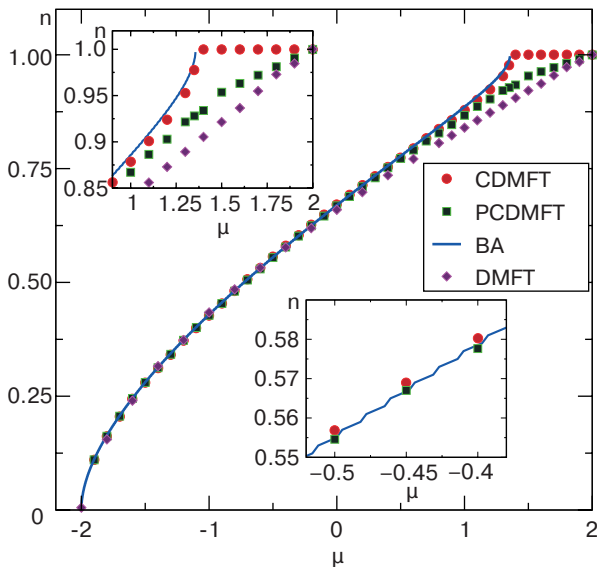
at intermediate coupling, weak-coupling and strong-coupling approaches give results that are nearly in quantitative agreement with each other. This gives us great confidence into the validity of the results. As an example of concordance, consider the fact that to obtain spectral weight near $(\pi/2, \pi/2)$ at optimal doping in the electron-doped systems, U has to be roughly $6t$. For larger U, ($U = 8t$ in CPT) that weight, present in the experiments, disappears. Smaller values of U ($U = 4t$ in CPT) do not lead to a pseudogap. Other examples of concordance include the value of the superconducting transition temperature T_c obtained with DCA and with TPSC as well as the temperature dependence of souble occupancy obtained with the same two methods.

3.1. Weak and strong-coupling pseudogap

To understand the pseudogap it is most interesting to consider both hole and electron-doped cuprates at once. This means that we have to include particle-hole symmetry breaking hoppings, t' and t''. We will see in the present section that it is possible to obtain a pseudogap at strong coupling without a large correlation length in the particle-hole or in the particle-particle channels. By contrast, at weak coupling one does need a long-correlation length and low dimension. So there appears to be theoretically two different mechanisms for the pseudogap.

3.1.1. Claster perturbation theory

The top panel in Fig. 19 presents the single-particle spectral weight, $A(\mathbf{k}, \omega)$ or imaginary part of the single-particle Green function, for the model with $t' = -0.3t$, $t'' = 0.2t$ in the hole-doped case, for about 17 doping [77]. Each curve is for a different wave vector (on a trajectory shown in the inset) and is plotted as a function of frequency in units of t. This kind of plot is known as energy dispersion curves (EDC). It is important to point out that the theoretical results are obtained by broadening a set of delta function, so that the energy resolution is $\eta = 0.12t$ corresponding roughly to the experimental resolution we will compare with in the next section. At small $U = 2t$ on the top panel of Fig. 19, one recovers a Fermi liquid. At large U, say $U = 8t$, the Mott gap at positive energy is a prominent feature. The pseudogap is a different feature located around the Fermi energy. To see it better, we present on the left-hand panel of Fig. 20 a blow-up in the vicinity of the Fermi surface crossing occurring near $(\pi,0)$. Clearly, there is a minimum in $A(\mathbf{k}, \omega)$ at the Fermi-surface crossing when U is large enough instead of a maximum like in Fermi liquid theory.

It is also possible to plot $A(\mathbf{k}, \omega)$ at fixed frequency for various momenta. They are so-called momentum
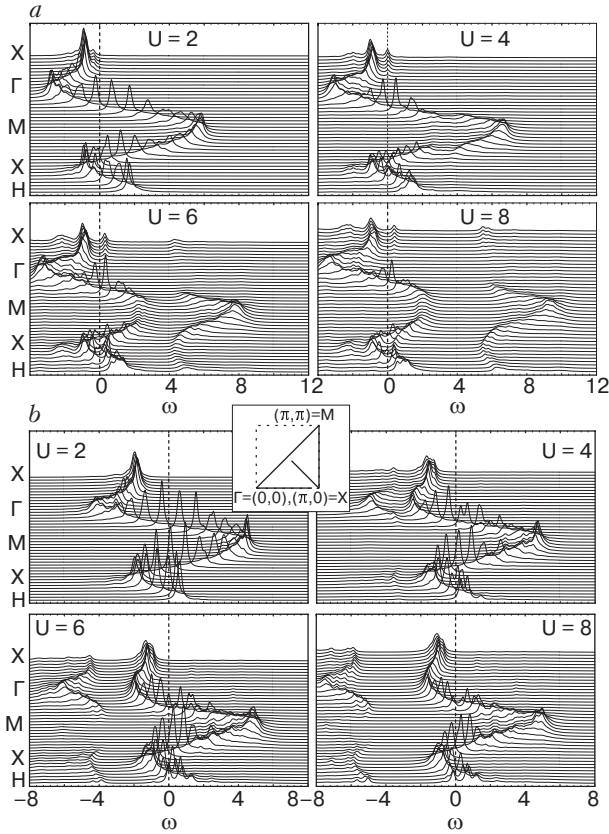

Fig. 18. CDMFT calculation on a 2×2 cluster with 8 bath sites of the density as a function of the chemical potential in the one-dimensional Hubbard model for $u = 4t$, as compared with the exact solution, DMFT and other approximation schemes. Taken from Ref. 74.

a

b

Fig. 19. Single particle spectral weight, as a function of energy ω in units of t, for wave vectors along the high-symmetry directions shown in the inset. CPT calculations on a 3×4 cluster with ten electrons (17 hole doped) (*a*); the same as (*a*), with 14 electrons (17 electron doped). In all cases $t' = -0.3t$ and $t'' = 0.2t$. A Lorentzian broadening $\eta = 0.12t$ is used to reveal the otherwise delta peaks (*b*). From Ref. 77.
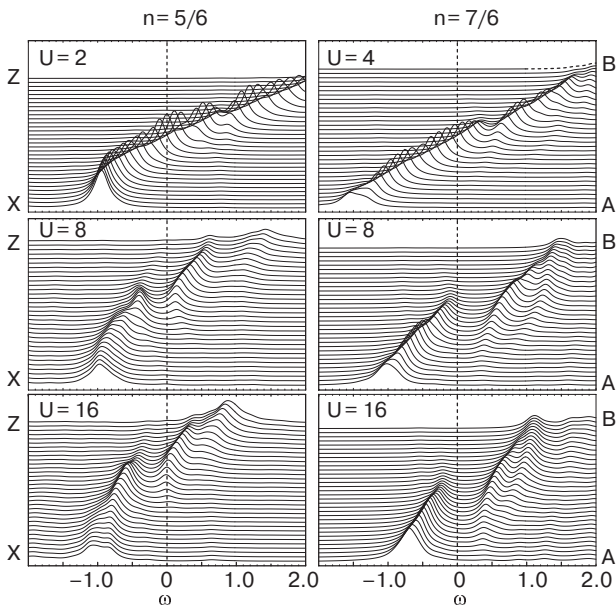

Fig. 20. Onset of the pseudogap as a function of U corresponding to Fig. 19, taken from Ref. 77. Hole-doped case on the left, electron-doped case on the right panel.
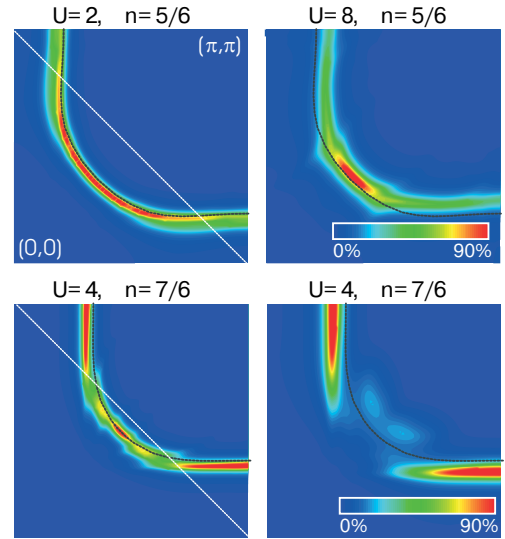

Fig. 21. MDC from CPT in the $t-t' = -0.3t$, $t'' = 0.2t$ Hubbard model, taken from Ref. 77.

dispersion curves (MDC). In Fig. 21 we take the Fermi energy $\omega = 0$, and we plot the magnitude of the single-particle spectral weight in the first quadrant of the Brillouin zone using red for high-intensity and blue for low intensity. The figure shows that, in the hole-doped case (top panel), weight near $(\pi/2, \pi/2)$ survives while it tends to disappear near $(\pi, 0)$ and $(0, \pi)$. That pseudogap phenomenon is due not only to large U but also to the fact that the line that can be drawn between the points $(\pi, 0)$ and $(0, \pi)$ crosses the Fermi surface. When there is no such crossing, one recovers a Fermi surface (not shown here). The $(\pi, 0)$ to $(0, \pi)$ line has a double role. It is the antiferromagnetic zone boundary, as well as the line that indicates where umklapp processes become possible, i.e., the line where we can scatter a pair of particles on one side of the Fermi surface to the other side with loss or gain of a reciprocal lattice vector. Large scattering rates explain the disappearance of the Fermi surface [77]. We also note that the size of the pseudogap in CPT, defined as the distance between the two peaks, does not scale like $J = 4t^2/U$ at large coupling. It seems to be very weakly U dependent, its size being related to t instead. This result is corroborated by CDMFT [67].

The EDC for the electron-doped case is shown on the bottom panels of Fig. 19 near optimal doping again. This time, the Mott gap appears below the Fermi surface so that the lower Hubbard band becomes accessible to experiment. The EDC in Fig. 22 shows very well both the Mott gap and the pseudogap. Details of that pseudogap can be seen both in the inset of Fig. 22 or on the right-hand panel of Fig. 20. While in the hole-doped case the MDC appeared to evolve continuously as we increase U (top panel of Fig. 21), in the electron-doped case (bottom panel)
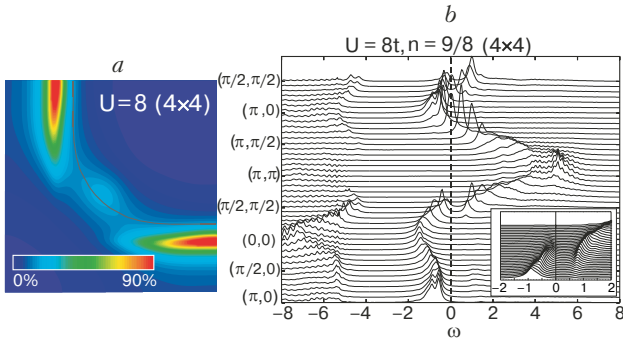
Fig. 22. The corresponding momentum distribution curve (*a*). EDC in the $t-t'-t''$ Hubbard model, calculated on a 16-site cluster in CPT, at $n = 9/8$. Inset: the pseudogap (*b*).

the weight initially present near $(\pi/2, \pi/2)$ at $U = 4t$ disappears by the time we reach $U = 8t$.

In Fig. 23 we show, with the same resolution as CPT, the MDC for VCPT [18]. In this case the effect of long-range order is included and visible but at this resolution, the results are not too different from those obtained from CPT in Fig. 21.

3.1.2. Cellular dynamical mean field theory and dynamical cluster approximation

CDMFT [16] gives MDC that, at comparable resolution, $\eta = 0.1t$, are again compatible with CPT and with VCPT. The middle panel in Fig. 24 is for the electron-doped case but with a particle-hole transformation so that $t' = +0.3t$ and $\mathbf{k} \rightarrow \mathbf{k} + (\pi, \pi)$. Since there is a non-zero d-wave order parameter in this calculation, improving the resolution to $\eta = 0.02t$ reveals the d-wave gap, as seen in the right most figure.

It has been argued for a while in DCA that there is a mechanism whereby short-range correlations at strong coupling can be the source of the pseudogap phenomenon [78]. To illustrate this mechanism in
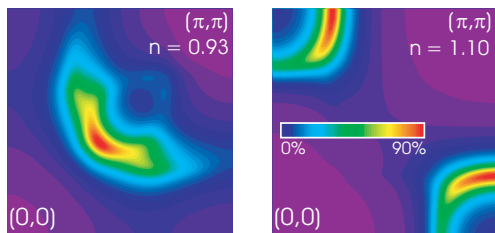

Fig. 23. EDC in the $t-t'-t''$ Hubbard model, with $t' = -0.3t$ and $t'' = 0.2t$, calculated on a 8-site cluster for $U = 8t$ in VCPT. d-wave superconductivity is present in the holde-doped case (left) and both antiferromagnetism and d-wave superconductivity in the electron-doped case. The resolution is not large enough in the latter case to see the superconducting gap. The Lorentzian broadening is $0.2t$. From Ref. 18.
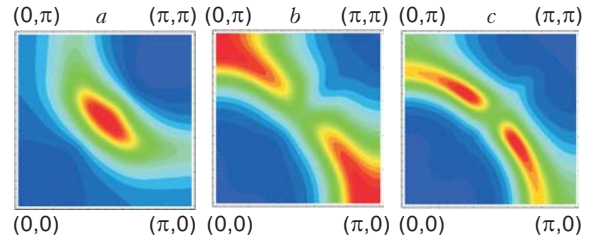

Fig. 24. MDC in the $t-t'$, $U = 8t$ Hubbard model, calculated on a 4-site cluster in CDMFT. Energy resolution, $\eta = 0.1t$ (*a*), (*b*). Hole-doped dSC ($t' = -0.3t, n = 0.96$) (*a*). Electron-doped dSC ($t' = 0.3t, n = 0.93$) (*b*) Same as middle with $\eta = 0.02t$. Note the particle-hole transformation in the electron-doped case (*c*). From Ref. 16.

CDMFT, we take the case $t' = t'' = 0$ and compare in Fig. 25 the EDC for $U = 8t$ without long-range order (top panels) and with long-range antiferromagnetic order (bottom panels) [67]. The four bands appearing in Figs. 25,*a* and 25,*d* are in agreement with what has been shown [73,79,80] with CPT, VCPT and QMC in Fig. 26. Evidently there are additional symmetries in the antiferromagnetic case. The bands that are most affected by the long-range order are those that are closest to the Fermi energy, hence they reflect spin correlations, while the bands far from the Fermi energy seem less sensitive to the presence of long-range order. These far away bands are what is left from the atomic limit where we have two dispersionless bands. As we dope, the chemical potential moves into the lower band closest to the Fermi energy. When there is no long-range order (Figs. 25,*b* and 25,*c*) the lower band closest to the Fermi energy moves very close to it, at the same time as the upper band closest to the Fermi energy looses weight, part of it moving closer to the Fermi energy. These two bands leave a pseudogap at the Fermi energy [81,82],
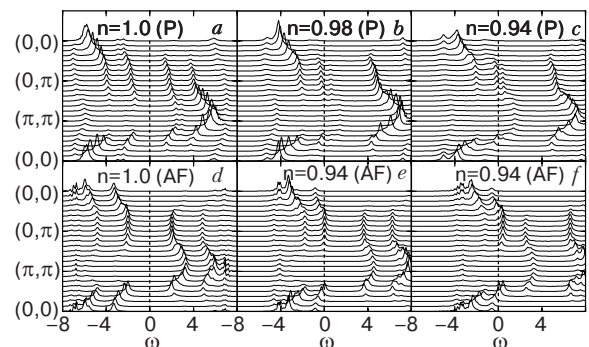

Fig. 25. EDC in the $t-t' = 0$, $U = 8t$ Hubbard model, calculated on a 4-site cluster in CDMFT. Top: normal (paramagnetic) state for various densities. Bottom: same for the antiferromagnetic state. From Ref. 65.
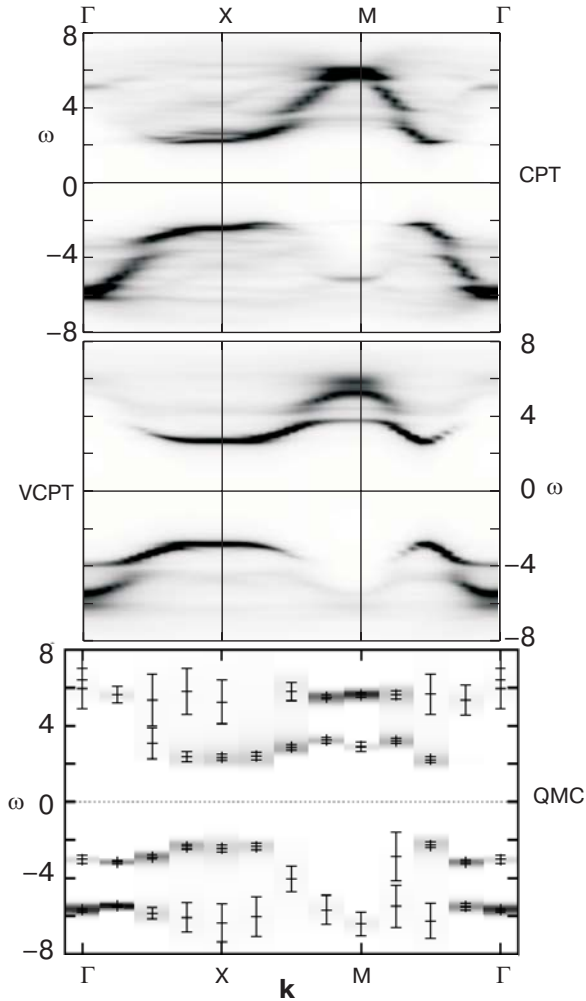
Fig. 26. EDC in the Hubbard model, $U = 8t$, $t' = 0$ calculated in CPT, VCPT and QMC. From Ref. 73.

Fig. 27. Double occupancy $\langle n_\uparrow n_\downarrow \rangle$, in the two-dimensional Hubbard model for $n = 1$, as calculated from TPSC (lines with x) and from DCA (symbols) from Ref. 84. Taken from Ref. 83.

although we cannot exclude that increasing the resolution would reveal a Fermi liquid at a very small energy scale. In the case when there is long-range antiferromagnetic order, (Figs. 25,*e* and 25,*f*) the upper band is less affected while the chemical potential moves in the lower band closest to the Fermi energy but without creating a pseudogap, as if we were doping an itinerant antiferromagnet. It seems that forcing the spin correlations to remain short range leads to the pseudogap phenomenon in this case. When a pseudogap appears, it is created again by very large scattering rates [67].

3.1.3. TPSC (including analytical results)

In Hartree–Fock theory, double occupancy is given by $n^2 / 4$ and is independent of temperature. The correct result does depend on temperature. One can observe in Fig. 27 the concordance between the results for the temperature-dependent double occupancy obtained with DCA and with TPSC [83] for the $t' = t'' = 0$ model. We have also done extensive
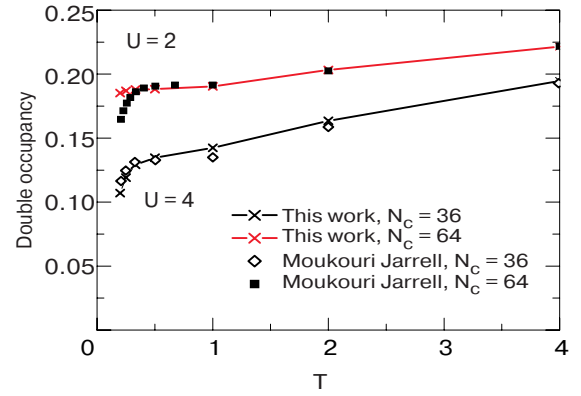
comparisons between straight QMC calculations and TPSC [39]. The downturn at low temperature has been confirmed by the QMC calculations. It comes from the opening of the pseudogap due to antiferromagnetic fluctuations, as we will describe below. The concomitant increase in the local moment corresponds to the decrease in double-occupancy. There seems to be a disagreement at low temperature between TPSC and DCA at $U = 2t$. In fact TPSC is closer to the direct QMC calculation. Since we expect quantum cluster methods in general and DCA in particular to be less accurate at weak coupling, this is not too worrisome. At $U = 4t$ the density of states obtained with TPSC and with DCA at various temperatures are very close to each other [83]. We stress that as we go to temperatures well below the pseudogap, TPSC becomes less and less accurate, generally overemphasizing the downfall in double occupancy.

We will come back to more details on the predictions of TPSC for the pseudogap, but to illustrate the concordance with quantum cluster results shown in the previous subsection, we show in Fig. 28 MDC obtained at the Fermi energy in the hole doped case for $t' = -0.175t$, $t'' = 0.05t$. Again there is quasi-particle weight near $(\pi/2, \pi/2)$ and a pseudogap near $(\pi, 0)$ and $(0, \pi)$. However, as we will discuss below, the
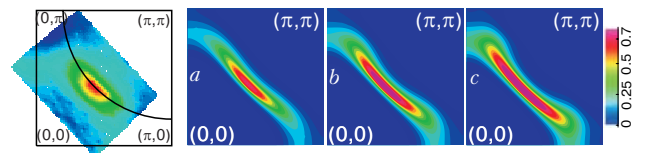

Fig. 28. MDC at the Fermi energy for the two-dimensional Hubbard model for $U = 6.25$, $t' = -0.175t$, $t'' = 0.05t$ at various hole dopings, as obtained from TPSC. The far left from Ref. 85 is the Fermi surface plot for 10 hole-doped $Ca_{2-x}Na_xCuO_2Cl_2$.
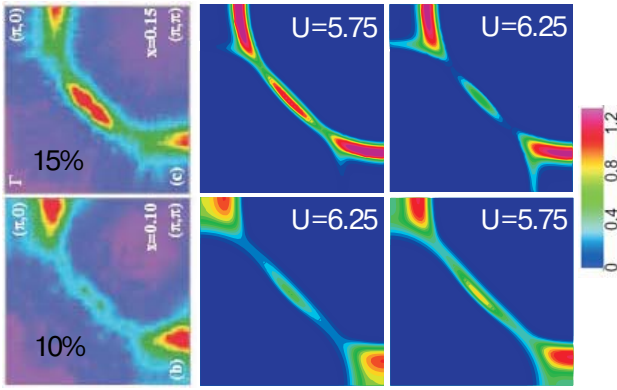
Fig. 29. MDC at the Fermi energy in the electron-doped case with $t' = -0.175t$, $t'' = 0.05t$ and two different U's, $U = 6.25t$ and $U = 5.75t$ obtained from TPSC. The first column is the corresponding experimental plots at 10 and 15 doping in Ref. 86. From Refs. 41,87.

antiferromagnetic correlation length necessary to obtain that pseudogap is too large compared with experiment. The electron-doped case is shown in Fig. 29 near optimal doping and for different values of U. As U increases, the weight near $(\pi/2, \pi/2)$ disappears. That is in concordance with the results of CPT shown in Fig. 21 where the weight at that location exists only for small U. That also agrees with slave-boson calculations [88] that found such weight for $U = 6t$ and it agrees also with one-loop calculations [89] starting from a Hartree−Fock antiferromagnetic state that did not find weight at that location for $U = 8t$. The simplest Hartree−Fock approach [20,90] yields weight near $(\pi/2, \pi/2)$ only for unreasonably small values of U.
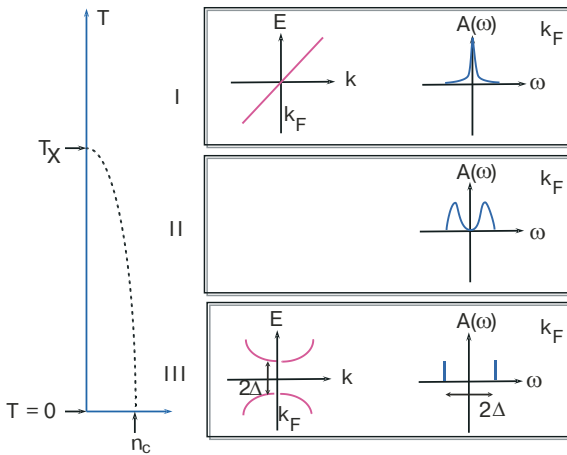

Fig. 30. Cartoon explanation of the pseudogap in the weak-coupling limit. Below the dahsed crossover line to the renormalized classical regime, when the antiferromagnetic correlation length becomes larger than the thermal de Broglie wave length, there appears precursors of the zero-temperature Bogoliubov quasiparticles for the long-range ordered antiferromagnet.

A cartoon explanation of the pseudogap is given in Fig. 30. At high temperature we have a Fermi liquid, as illustrated in panel I. Now, suppose we start from a ground state with long-range order as in panel III, in other words at a filling between half-filling and n_c. In the Hartree−Fock approximation we have a gap and the fermion creation-annihilation operators now project on Bogoliubov−Valentin quasiparticles that have weight at both positive and negative energies. In two dimensions, the Mermin−Wagner theorem means that as soon as we raise the temperature above zero, long-range order disappears, but the antiferromagnetic correlation length ξ remains large so we obtain the situation illustrated in panel II, as long as ξ is much larger than the thermal de Broglie wave length $\xi_{\text{th}} \equiv v_F/(\pi T)$ in our usual units. At the crossover temperature T_X then the relative size of ξ and ξ_{th} changes and we recover the Fermi liquid. We now proceed to sketch analytically where these results come from starting from finite temperature. Details and more complete formulae may be found in Refs. 22,23,31,32. Note also that a study starting from zero temperature has also been performed in Ref. 91.

First we show how TPSC recovers the Mermin−Wagner theorem. Consider the self-consistency conditions given by the local moment sum rule Eq. (4) together with the expression for the spin-susceptibility Eq. (2) and U_{sp} in Eq. (5). First, it is clear that if the left -hand side of the local moment sum rule Eq. (4) wants to increase because of proximity to a phase transition, the right-hand side can do so only by decreasing $\langle n_\uparrow n_\downarrow \rangle$ which in turns decreases U_{sp} through Eq. (5) and moves the system away from the phase transition. This argument needs to be made more precise to include the effect of dimension. First, using the spectral representation one can show that every term of $\chi_{\text{sp}}(\mathbf{q}, iq_n)$ is positive. Near a phase transition, the zero Matsubara frequency component of the susceptibility begins to diverge. On can check from the real-time formalism that the zero-Matsubara frequency contribution dominates when the characteristic spin fluctuation frequency $\omega_{\text{sp}} \sim \xi^{-2}$ becomes less than temperature, the so-called renormalized-classical regime. We isolate this contribution on the left-hand side of the local moment sum rule and we move the contributions from the non-zero Matsubara frequencies, that are non-divergent, on the right-hand side. Then, converting the wave vector sum to an integral and expanding the denominator of the susceptibility around the wave vector where the instability would occurs to obtain an Ornstein−Zernicke form, the local moment sum rule Eq. (4) can be written in the form

$$T \int \frac{q^{d-1}dq}{q^2 + \xi^{-2}} = C(T). \qquad (28)$$

The constant on the right-hand side contains only non-singular contributions and ξ^{-2} contains U_{sp} that we want to find. From the above equation, one finds immediately that in $d = 2$, $\xi \approx \exp(C(T)/T)$ so that the correlation length diverges only at $T = 0$. In three dimensions, isotropic or not, exponents correspond to those of the $N = \infty$ universality class [45].

To see how the pseudogap opens up in the single-particle spectral weight, consider the expression (6) for the self-energy. Normally one has to do the sum over bosonic Matsubara frequencies first, but the zero Matsubara frequency contribution has the correct asymptotic behavior in fermionic frequencies ik_n so that one can once more isolate on the right-hand side the zero Matsubara frequency contribution. This is confirmed by the real-time formalism [22] (See also Eq. (35) below). In the renormalized classical regime then, we have

$$\Sigma(\mathbf{k}_F, ik_n) \propto T \int q^{d-1}dq \frac{1}{q^2 + \xi^{-2}} \frac{1}{ik_n - \varepsilon_{\mathbf{k}_F + \mathbf{Q} + \mathbf{q}}} \qquad (29)$$

where $\mathbf{Q}$ is the wave vector of the instability. Hence, when $\varepsilon_{\mathbf{k}_F + \mathbf{Q}} = 0$, in other words at hot spots, we find after analytical continuation and dimensional analysis that
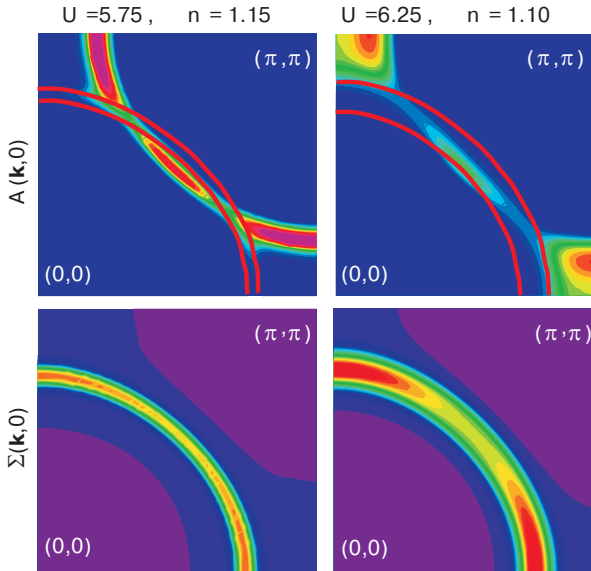
U =5.75 ,   n = 1.15   U =6.25 ,   n = 1.10

Fig. 31. MDC plots at the Fermi energy (upper) and corresponding scattering rates (lower) obtained from TPSC. The semicircular dark gray (red) lines on the upper panel indicate the region where the scattering rate in the corresponding lower panels is large.

$$\text{Im} \, \Sigma^R(\mathbf{k}_F, 0) \propto -\pi T \int \frac{d^{d-1}q_\perp dq_\parallel}{q_\perp^2 + q_\parallel^2 + \xi^{-2}} \times$$

$$\times \delta(v_F' q_\parallel) \propto \frac{\pi T}{v_F'} \xi^{3-d}. \qquad (30)$$

Clearly, in $d = 4$, $\text{Im} \, \Sigma^R(\mathbf{k}_F, 0)$ vanishes as temperature decreases, $d = 3$ is the marginal dimension and in $d = 2$ we have that $\text{Im} \, \Sigma^R(\mathbf{k}_F, 0) \propto \xi/\xi_{th}$ that diverges at zero temperature. In a Fermi liquid that quantity vanishes at zero temperature. A diverging $\text{Im} \, \Sigma^R(\mathbf{k}_F, 0)$ corresponds to a vanishingly small $A(\mathbf{k}_F, \omega = 0)$ as we can see from

$$A(\mathbf{k}, \omega) = \frac{-2 \, \text{Im} \, \Sigma^R(\mathbf{k}_F, \omega)}{(\omega - \varepsilon_{\mathbf{k}} - \text{Re} \, \Sigma^R(\mathbf{k}_F, \omega))^2 + \text{Im} \, \Sigma^R(\mathbf{k}_F, \omega)^2}. \qquad (31)$$

To see graphically this relationship between the location of the pseudogap and large scattering rates at the Fermi surface, we draw in Fig. 31 both the Fermi surface MDC and, in the lower panels, the corresponding plots for $\text{Im} \, \Sigma^R(\mathbf{k}, 0)$. Note that at stronger U the scattering rate is large over a broader region, leading to a depletion of $A(\mathbf{k}, \omega)$ over a broader range of $\mathbf{k}$ values.

An argument for the splitting in two peaks seen in Figs. 6 and 30 is as follows. Consider the singular renormalized contribution coming from the spin fluctuations in Eq. (29) at frequencies $\omega \gg v_F \xi^{-1}$. Taking into account that contributions to the integral come mostly from a region $q \leq \xi^{-1}$, this expression leads to

$$\text{Re} \, \Sigma^R(\mathbf{k}_F, \omega) = \left(T \int q^{d-1}dq \frac{1}{q^2 + \xi^{-2}} \right) \frac{1}{ik_n - \varepsilon_{\mathbf{k}_F + \mathbf{Q}}} \equiv$$

$$\equiv \frac{\Delta^2}{\omega - \varepsilon_{\mathbf{k}_F + \mathbf{Q}}} \qquad (32)$$

which, when substituted in the expression for the spectral weight (32) leads to large contributions when

$$\omega - \varepsilon_{\mathbf{k}} - \frac{\Delta^2}{\omega - \varepsilon_{\mathbf{k}_F + \mathbf{Q}}} = 0 \qquad (33)$$

or, equivalently,

$$\omega = \frac{(\varepsilon_{\mathbf{k}} + \varepsilon_{\mathbf{k}_F + \mathbf{Q}}) \pm \sqrt{(\varepsilon_{\mathbf{k}} - \varepsilon_{\mathbf{k}_F + \mathbf{Q}})^2 + 4\Delta^2}}{2}, \qquad (34)$$

which corresponds to the position of the hot spots in Fig. 29 for example.

Note that analogous arguments hold for any fluctuation that becomes soft [22], including superconduct-

ing ones [43,44]. The wave vector **Q** would be different in each case.

3.1.4. Weak- and strong-coupling pseudogaps

The CPT results of Figs. 19 and 22 clearly show that the pseudogap is different from the Mott gap. At finite doping, the Mott gap remains a local phenomenon, in the sense that there is a region in frequency space that is not tied to $\omega = 0$ where *for all wave vectors* there are no states. The peudogap by contrast is tied to $\omega = 0$ and occurs in regions nearly connected by (π, π), whether we are talking about hole- or about electron-doped cuprates. That the phenomenon is caused by short-range correlations can be seen in CPT from the fact that the pseudogap is independent of cluster shape and size (most of the results were presented for 3×4 clusters and we did not go below size 2×2). The antiferromagnetic correlations and any other two-particle correlations do not extend beyond the size of the lattice in CPT. Hence, the pseudogap phenomenon cannot be caused by antiferromagnetic long-range order since no such order exists in CPT. This is also vividly illustrated by the CDMFT results in Fig. 25 that contrast the case with and without antiferromagnetic long-range order. The CDMFT results also suggest that the pseudogap appears in the bands that are most affected by antiferromagnetic correlations hence it seems natural to associate it with short-range spin correlations. The value of t' has an effect, but it mostly through the fact that it has a strong influence on the relative location of the antiferromagnetic zone boundary and the Fermi surface, a crucial factor determining where the pseudogap is. All of this as well as many results obtained earlier by DCA [78] suggest that there is a strong coupling mechanism that leads to a pseudogap in the presence of only short-range two-body correlations. However, the range cannot be zero. Only the Mott gap appears at zero range, thus the pseudogap is absent in single-site DMFT.

In the presence of a pseudogap at strong coupling ($U > 8t$), wave vector is not, so to speak, such a bad quantum number in certain directions. In other words the wave description is better in those directions. In other directions that are «pseudogapped», it is as if the localized, or particle description was better. This competition between wave and particle behavior is inherent to the Hubbard model. At the Fermi surface in low dimension, it seems that this competition is resolved by dividing (it is a crossover, not a real division) the Fermi surface in different sections.

There is also a weak-coupling mechanism for the pseudogap. This has been discussed at length just in the previous section on TPSC. Another way to re-phrase the calculations of the previous section is in the real frequency formalism. There one finds [22] that

$$\Sigma''^R(\mathbf{k}_F, \omega) \propto \int \frac{d^{d-1}q_\perp}{(2\pi)^{d-1}} \int \frac{d\omega'}{\pi} [n(\omega') + f(\omega + \omega')] \times$$
$$\times \chi''_{sp}(\mathbf{q}; \omega') \qquad (35)$$

so that if the characteristic spin fluctuation frequency in $\chi''_{sp}(\mathbf{q}; \omega')$ is much larger than temperature, then $[n(\omega') + f(\omega + \omega')]$ can be considered to act like a window of size ω or T and $\chi''_{sp}(\mathbf{q}; \omega')$ can be replaced by a function of $\mathbf{q}$ times ω' which immediately leads to the Fermi liquid result $[\omega^2 + (\pi T)^2]$. In the opposite limit where the characteristic spin fluctuation frequency in $\chi''_{sp}(\mathbf{q}; \omega')$ is much less than temperature, then it acts as a window narrower than temperature and $[n(\omega') + f(\omega + \omega')]$ can be approximated by the low frequency limit of the Bose factor, namely T / ω'. Using the thermodynamic sum rule, that immediately leads to the result discussed before in Eq. (30), $\text{Im} \Sigma(\mathbf{k}_F, 0) \propto (\pi T / v_{F'}) \xi^{3-d}$. This mechanism for the pseudogap needs long correlation lengths. In CPT, this manifests itself by the fact that the apparent pseudogap in Fig. 21 at $U = 4t$ is in fact mostly a depression in spectral weight that depends on system size and shape. In addition, in contrast to the short-range strong-coupling mechanism, at weak coupling the pseudogap is more closely associated with the intersection of the antiferromagnetic zone boundary with the Fermi surface.

Which mechanism is important for the cuprates will be discussed below in the section on comparisons with experiments.

3.2. d-wave superconductivity

The existence of d-wave superconductivity at weak coupling in the Hubbard model mediated by the exchange of antiferromagnetic fluctuations [92,93] had been proposed even before the discovery of high-temperature superconductivity [6–8]. At strong-coupling, early papers [12,13] also proposed that the superconductivity would be d-wave. The issue became extremely controversial, and even recently papers have been published [11] that suggest that there is no d-wave superconductivity in the Hubbard model. That problem could have been solved very long ago through QMC calculations if it had been possible to do them at low enough temperature. Unfortunately, the sign problem hindered these simulations, and the high temperature results [5,46,94,95] were not encouraging: the d-wave susceptibility was smaller than for the non-interacting case. Since that time, numerical results from variational QMC [4,96], exact diagonalization [15] and other numerical approaches [97]

for example, suggest that there is indeed *d*-wave superconductivity in the Hubbard model.

In the first subsection, we show that VCPT leads to a zero-temperature phase diagram for both hole and electron-doped systems that does show the basic features of the cuprate phase diagram, namely an antiferromagnetic phase and a *d*-wave superconducting phase in doping ranges that are quite close to experiment [18]. (The following section will treat in more detail comparisons with experiment.) The results are consistent with CDMFT [16]. The fall in the *d*-wave superconducting order parameter near half-filling is associated with the Mott phenomenon. The next subsection stresses the instability towards *d*-wave superconductivity as seen from the normal state and mostly at weak coupling. We show that TPSC can reproduce available QMC results and that its extrapolation to lower temperature shows *d*-wave superconductivity in the Hubbard model. The transition temperature found at optimal doping [41] for $U = 4t$ agrees with that found by DCA [17], a result that could be fortuitous. But again the concordance between theoretical results obtained at intermediate coupling with methods that are best at opposite ends of the range of coupling strengths is encouraging.

3.2.1. Zero-temperature phase diagram

In VCPT, one adds to the cluster Hamiltonian the terms [18]

$$H'_M = M \sum_\mu e^{i\mathbf{Q}\cdot\mathbf{R}_\mu} (n_{\mu\uparrow} - n_{\mu\downarrow}),$$ (36)

$$H'_D = D \sum_{\mu\nu} g_{\mu\nu}(c_{\mu\uparrow}c_{\nu\downarrow} + \text{h.c.})$$ (37)

with M and D are respectively antiferromagnetic and *d*-wave superconducting Weiss fields that are determined self-consistently and $g_{\mu\nu}$ equal to ±1 on near-neighbor sites following the *d*-wave pattern. We recall that the cluster Hamiltonian should be understood in a variational sense. Figure 32 summarizes, for various cluster sizes, the results for the *d*-wave order parameter D_0 and for the antiferromagnetic order parameter M_0 for a fixed value of $U = 8t$ and the usual hopping parameters $t' = -0.3t$ and $t'' = 0.2t$. The results for antiferromagnetism are quite robust and extend over ranges of dopings that correspond quite closely to those observed experimentally. Despite the fact that the results for *d*-wave superconductivity still show some size dependence, it is clear that superconductivity alone without coexistence extends over a much broader range of dopings on the hole-doped than on the electron-doped side as observed experimentally. VCPT calculations
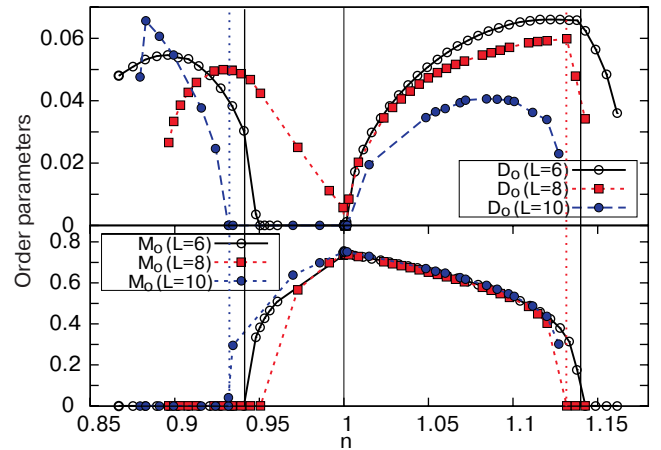

Fig. 32. Antiferromagnetic (bottom) and *d*-wave (top) order parameters for $U = 8t$, $t' = -0.3t$ $t'' = 0.2t$ as a function of the electron density (n) for 2×3, 2×4 and 10-site clusters, calculated in VCPT. Vertical lines indicate the first doping where only *d*-wave order is non-vanishing. From Ref. 18.

on smaller system sizes [98] but that include, for thermodynamic consistency, the cluster chemical potential as a variational parameter show superconductivity that extends over a much broader range of dopings. Also, for small 2×2 clusters, VCPT has stronger order parameter on the electron than on the hole-doped side, contrary to the results for the largest system sizes in Fig. 32. This is also what is found in CDMFT as can be seen in Fig. 33. It is quite likely that the zero-temperature Cooper pair size is larger than two sites, so we consider the results for 2×2 systems only for their qualitative value.

Concerning the question of coexistence with antiferromagnetism, one can see that it is quite robust on the electron-doped side whereas on the hole-doped
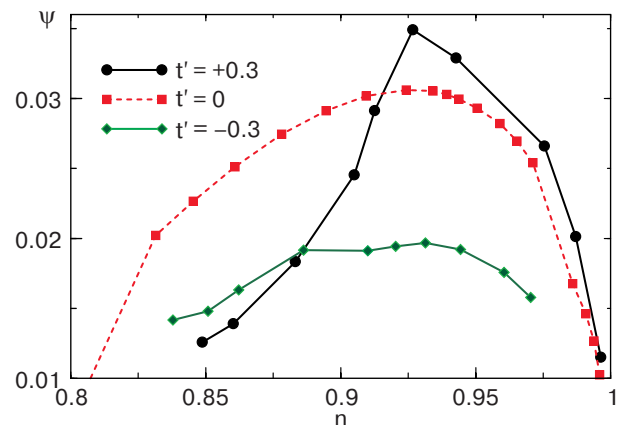

Fig. 33. *d*-wave order parameter as a function of n for various values of t', calculated in CDMFT on a 2×2 cluster for $U = 8t$. The positive t' case corresponds to the electron-doped case when a particle-hole transformation is performed. From Ref. 16.
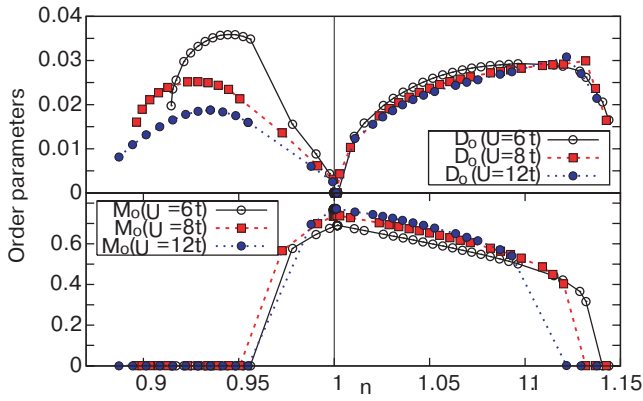
Fig. 34. Antiferromagnetic (bottom) and *d*-wave (top) order parameters as a function of the electron density (*n*) for $t' = -0.3t$ $t'' = 0.2t$ and various values of U on a 8-site cluster, calculated in VCPT. From Ref. 18.

side, it is size dependent. That suggests that one should also look at inhomogeneous solutions on the hole-doped side since stripes are generally found experimentally near the regions where antiferromagnetism and superconductivity meet.

Fig. 34 shows clearly that at strong coupling the size of the order parameter seems to scale with J, in other words it decreases with increasing U. This is also found in CDMFT [16], as shown in Fig. 35 for $t' = t'' = 0$.

If we keep the antiferromagnetic order parameter to zero, one can check with both VCPT and CDMFT (Fig. 34) that the *d*-wave superconducting order parameter goes to zero at half-filling. This is clearly due to Mott localization. Indeed, at smaller $U = 4t$ for example, the order parameter does not vanish at half-filling if we do not allow for long-range antiferromagnetic order, as illustrated in Fig. 35 for CDMFT [16]. The same result was found in VCPT, as shown in Fig. 36 [18]. Restoring long-range antiferro-
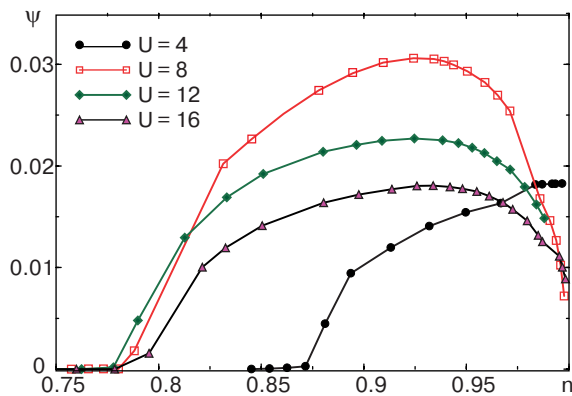

Fig. 35. *d*-wave order parameter as a function of *n* for various values of *U*, and $t' = t'' = 0$ calculated in CDMFT on a 4-site cluster. From Ref. 16.
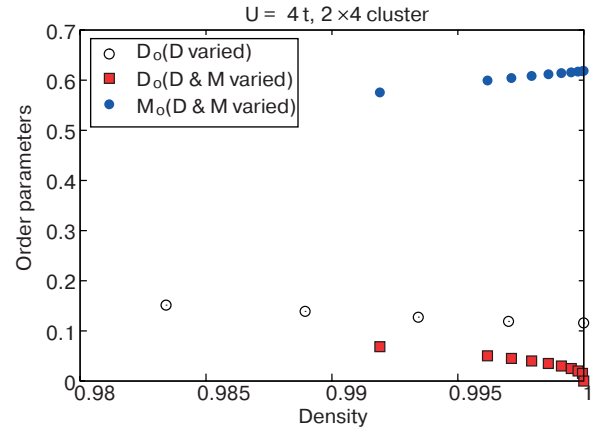

Fig. 36. VCPT calculations for $U = 4t, t' = t'' = 0$ near half-filling on 2×4 lattice. Contrary to the strong coupling case, the *d*-wave order parameter D_0 survives all the way to half-filling at weak coupling, unless we also allow for antiferromagnetism.

magnetic order does however make the *d*-wave order parameter vanish at half-filling.

There are thus two ways to make *d*-wave superconductivity disappear at half-filling, either through long antiferromagnetic correlation lengths [99] or through the Mott phenomenon. In the real systems, that are Mott insulators and also antiferromagnets at half-filling, both effects can contribute.

3.2.2. Instability of the normal phase

In the introduction to this section, we alluded to QMC calculations for the *d*-wave susceptibility [5,46,94,95]. Recent results [41] for that quantity as a function of doping for various temperatures and for $U = 4t$, $t' = t'' = 0$ are shown by symbols in Fig. 8. For lower temperatures, the sign problem prevents the calculation near half-filling. Yet, the lowest temperature is low enough that a dome shape begins to appear. Nevertheless, comparison with the non-interacting case, shown by the top continuous line, leads one to believe that interactions only suppress *d*-wave superconductivity. We can easily understand why this is so. As we already know, the TPSC results obtained from Eq. (7) are very close to the QMC calculations, as shown by the solid lines in Fig. 8. In the temperature range of interest, the main contribution comes from the first term in Eq. (7). That term represents the contribution to the susceptibility that comes from dressed quasiparticles that do not interact with each other. Since dressed quasiparticles have a lifetime, a pair breaking effect, it is normal that this contribution to the interacting susceptibility leads to a smaller contribution than in the non-interacting case. At the lowest temperature, $\beta = 4/t$, the vertex contribution represented by the second term in

Eq. (7) accounts for about 20% of the total. It goes in the direction of increasing the susceptibility. As we decrease the temperature further in TPSC, that term becomes comparable with the first one. Since the vertex in Eq. (7) accounts for the exchange of a single spin wave, equality with the first term signals the divergence of the series, as in $1/(1 - x) \sim 1 + x$. The divergence of that series represents physically the instability of the normal phase to a d-wave super-conducting phase. This is analogous to the Thouless criterion and hence it gives an upper bound to T_c. In other words, Berezinskii-Kosterlitz-Thouless physics is not included.

Fig. 37 shows the TPSC transition temperature for $U = 4t$ and for $U = 6t$. As we move towards half-fill-ing, located to the left of the diagram, starting from large dopings, T_c goes up because of the increase in antiferromagnetic fluctuations. Eventually, T_c turns around and decreases because of the opening of the pseudogap. Physically, when the pseudogap opens up, weight is removed from the Fermi level, the density of states becomes very small, and pairing cannot occur any more. In the FLEX approximation [21,100] that does not exhibit a pseudogap [101], that downturn, observed already in QMC at high temperature, does not occur. We have observed that in cases where $t' \neq 0$ so that the pseudogap opens only in a limited region around hot spots, the downturn can become less pro-nounced.

The case $n = 0.9 = 1 - \delta$ that corresponds to optimal doping for $U = 4t$ in Fig. 37 has been studied by DCA. In an extensive and systematic study of the size dependence, Maier et al. [17] established the existen-ce of a d-wave instability at a temperature that coincides to within a few percent with the result in Fig. 37. Since very few vortices can fit within even the largest cluster sizes studied in Ref. 17, it is quite
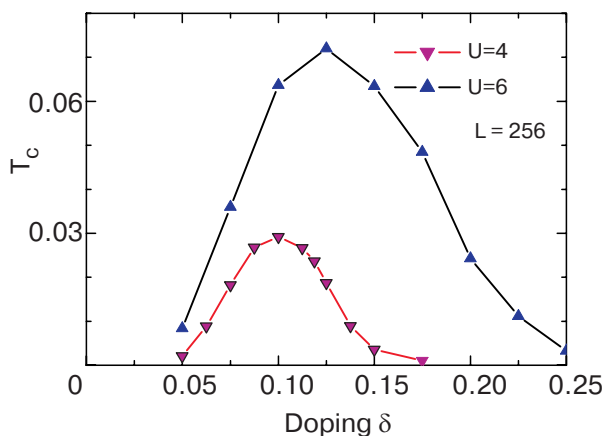

Fig. 37. T_c as a function of doping, $\delta = 1 - n$, for $t' = t'' = 0$ calculated in TPSC using the Thouless criterion. From Ref. 41.

likely that the T_c that they find does not include Berezinskii−Kosterlitz−Thouless effects, just like ours. Despite the fact that, again, the concordance between weak and strong coupling methods at inter-mediate coupling comforts us, the uncertainties in the results found with TPSC and DCA force us to also allow for a fortuitous coincidence.

4. Comparisons with experiment

The reduction of the real problem of high-tempera-ture superconducting materials to a one-band Hub-bard is a non-trivial one. It has been discussed already in the early days of high T_c superconductivity. The no-tion of a Zhang-Rice singlet [102] emerged for hole doped systems. The mapping to a one-band model has been discussed in many references [103,104], and we do not wish to discuss this point further here. In fact it is far from obvious that this mapping is possible. It is known that about 0.5 eV below the Fermi surface, that mapping fails in hole-doped systems [104]. Neverthe-less, the one-band Hubbard model is in itself a hard enough problem for us. So it is satisfying to see that, in the end, it gives a picture that agrees with experi-ment in a quite detailed manner for the ARPES spec-trum near the Fermi surface, for the phase diagram as well as for neutron scattering in cases where it can be calculated.

Although we will not come back on this point at all, we briefly mention that fitting the spin wave spec-trum [105] for all energies and wave vectors at half filling in La_2CuO_4 gives values of U, t, t', t'' that are close to those used in the rest of this paper [106−109]. It is in this context that ring exchange terms are usu-ally discussed.

4.1. ARPES spectrum, an overview

ARPES experiments have played a central role in the field of high-temperature superconductivity. We cannot expect to be able to present the vast experi-mental literature on the subject. We refer the reader to a very exhaustive review [110] and to some less complete but recent ones [111,112]. The main facts about ARPES have been summarized in Ref. 110. We comment on their main points one by one, using italics for our paraphrase of the reported experimental obser-vations.

(i) *The importance of Mott Physics and the renormalization of the bandwidth from t to J for the undoped parent compounds*. This renormalization was clear already in early QMC calculations [80,113]. We already discussed the presence of four peaks. The one nearest to the Fermi surface at negative energies is the one referred to by experimentalists when they refer to

this renormalization. This band has a dispersion of order J (not shown on Fig. 26, but see Ref. 113). This result also agrees with VCPT as shown in Fig. 26 and CDMFT (Fig. 25,*a*). As shown in Figs. 25,*a* and 25,*d*, whether the state is ordered or not the band width is similar. Analytical strong-coupling expansions [114,115] and exact diagonalizations also find the same result. To find detailed agreement with experiment, one needs to include t' and t'' [116]. The evolution of the position of chemical potential for extremely small dopings as discussed in Ref. 117 is not reproduced by the strong-coupling calculations, although the result on chemical potential is somewhat material dependent [118].

(ii) *In the overdoped case, the Fermi surface is well defined.* Although we have not shown any figures concerning this point, VCPT and CDMFT show the same result.

(iii) *The evolution with doping of the electronic structure has been mapped. It has shown the importance of antiferromagnetic correlations in the p-type underdoped cuprates and especially in the n-type ones in which the hot-spot physics is still observed at optimal doping.* We will come back on the latter point for electron-doped cuprates in the following subsection. The strong-coupling results obtained with VCPT and CDMFT have a resolution of order $0.1t$, which translates into about 30 meV. This is not enough to accurately measure the Fermi velocity, which was found to be doping independent in LSCO [119]. However, this suffices to compare with MDC curves obtained experimentally by integrating over an energy range of about 60 meV, as shown in Fig. 38 obtained in Ref. 85 on Calcium oxyclorate $Ca_{2-x}Na_xCuO_2Cl_2$, a 10 hole-doped high temperature superconductor. The similarities between that figure and the CPT (Fig. 21), VCPT (Fig. 23) and CDMFT (Fig. 24) results is striking. The agreement is better when no antiferromagnetic long-range order is assumed, as in the CPT case. The flattening of the band structure near $(\pi,0)$ observed experimentally, can also be seen in CPT by comparing the top and middle EDC's taken at small and large U respectively on the left panel of Fig. 20. This flattening is associated with the pseudogap phenomenon. Recall that the theoretical results were obtained with $t' = -0.3t$ and $t'' = 0.2t$. This in turn implies an electron-hole asymmetry that is observed experimentally. We come back to this in the following subsection.

(iv) *The overall d-wave symmetry of the superconducting gap has been observed for both hole and electron doping, supporting the universality of the pairing nature in the cuprates.* In the next to next subsection, we discuss the phase diagram for com-
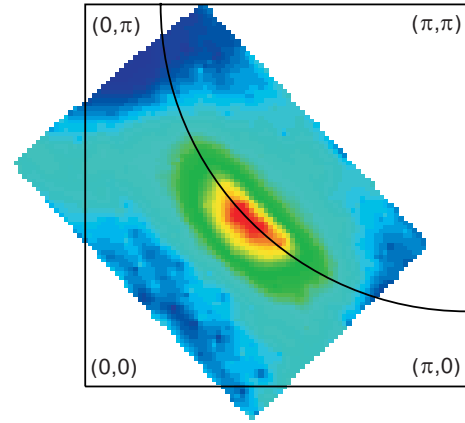

Fig. 38. MDC at the Fermi energy for 10 hole-doped $Ca_{2-x}Na_xCuO_2Cl_2$ from Ref. 85.

peting antiferromagnetism and d-wave superconductivity and show striking similarities with the observations.

(v) *A normal-state pseudogap has been observed to open up at a temperature $T^* > T_c$ in the underdoped regime with a d-wave form similar to the one of the superconducting gap.* That statement is correct only in the hole-doped compounds. In electron-doped systems the pseudogap has a form that is not of d-wave shape. If T_c comes from a universal pairing mechanism, a universal mechanism may also be behind the pseudogap. As we have already discussed however, there are quantitative differences between strong and weak coupling mechanisms for both T_c and the pseudogap. For electron-doped systems, we made quantitative predictions for the value of T^* that have later been confirmed experimentally. All this is discussed further below. To date, in cluster methods the pseudogap temperature has been studied only with DCA [78].

(vi) *A coherent quasiparticle peak below T_c has been observed near $(\pi,0)$ whose spectral weight scales with the doping level x in the underdoped regime.* We expect that it is a general result that long-range order will restore quasiparticle like excitations in strongly correlated systems because gaps remove scattering channels near the Fermi level. This is clearly illustrated by comparing the upper and lower panels in Fig. 25 that contrast the same spectra with and without antiferromagnetic long-range order. We have not performed the analysis of our results yet that could tell us whether the spectral weight of the quasiparticle scales with x in the hole-underdoped regime. Our resolution may not be good enough to see the quasiparticle peak. Sharpening of the quasiparticle excitations in the superconducting state has however been observed in DCA [120].

(vii) *The presence of an energy scale of about* 40 – 80 meV *in the quasiparticle dynamics manifests itself through a sharp dispersion renormalization and drop in the scattering rate observed at those energies at different momenta.* In hole-doped systems there is a kink in the nodal direction that is already seen above T_c while in the antinodal direction it appears only below T_c. The energy scales and doping dependences of these two kinks are also different [121]. The energy resolution in VCPT and CDMFT is not sufficient to distinguish these subtleties. In electron-doped cuprates experiments [122] suggest that there is no observable kink feature, in agreement with the results presented in the following subsection.

4.2. The pseudogap in electron-doped cuprates

The ARPES spectrum of electron-doped cuprates is strikingly different from that of their hole-doped counterpart. The Fermi energy MDC's for the first quadrant of the Brillouin zone [86] are shown at the top of Fig. 39 for three different dopings. There is a very clear evolution with doping. At the lowest dopings, there is no weight near $(\pi/2, \pi/2)$, contrary to the hole-doped case shown in Fig. 38. For all dopings there is weight near $(\pi, 0)$ instead of the pseudogap that appeared there in the hole-doped case. The EDC's, also shown on the bottom of Fig. 39, are drawn for a trajectory in the Brillouin zone that follows what would be the Fermi surface in the
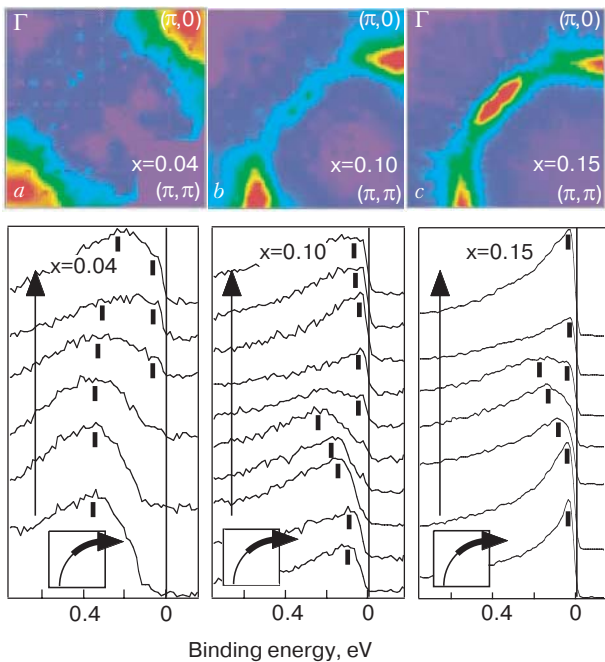

Fig. 39. Doping dependence of the MDC from experiments on NCCO with the corresponding EDC. From Ref. 86.
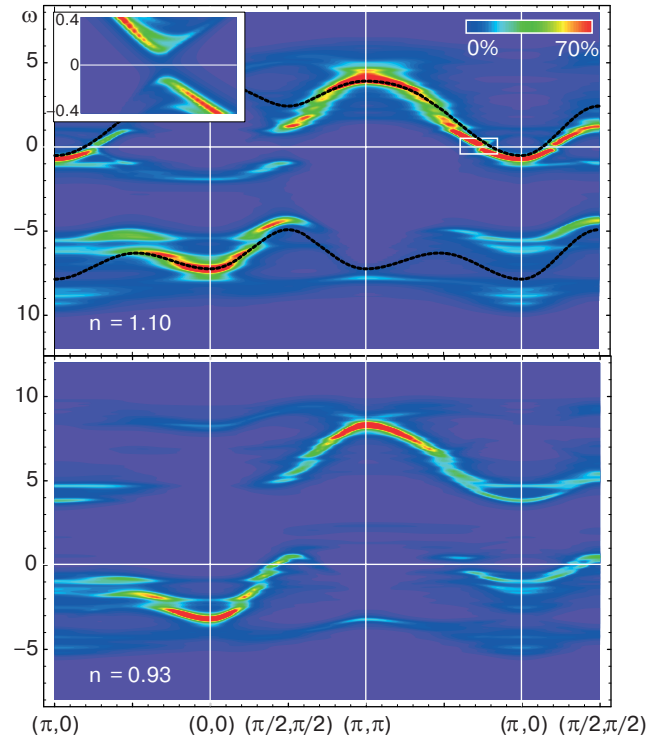

Fig. 40. Intensity plot of the spectral function as a function of ω in units of t and wave vector from VCPT for $U = 8t$ $t' = -0.3t$, $t'' = 0.2t$ and $n = 0.93$ at the bottom and $n = 1.10$ (electron-doped) at the top. The Lorentzian broadening is $0.12t$ in the main figure and $0.04t$ in the inset that displays the d-wave gap. Top panel is for the electron-doped case in the right-hand panel of Fig. 23, while bottom panel is for the hole-doped case on the left of Fig. 23. From Ref. 18.

non-interacting case. The oval and semioval regions on the corresponding MDC's along that trajectory are referred to as hot spots. On the EDC's we clearly see that hot spots do not correspond to simply a decrease in the quasiparticle weight Z. They truly originate from a pseudogap, in other words from the fact that the maximum is pushed away from zero energy. Even though the measurements are done at low temperature ($T = 10$–20 K) the energy resolution of about 60 meV makes the superconducting gap invisible. What is observed at this resolution is the pseudogap.

The contrast between the location of the pseudogap in the hole and electron-doped compounds is clearly seen in Fig. 40 obtained from VCPT [18]. In that figure, the magnitude of the spectral weight is represented by the different colors as a function of frequency (in units of t) along different cuts of the Brillouin zone. In the bottom panel, for the hole-doped case, one observes the pseudogap near $(\pi, 0)$. In the top panel, for the electron-doped case, it is only by zooming (inset) on the region for the Fermi energy

crossing near $(\pi,0)$ that one sees the *d*-wave super-conducting gap. At 10% electron-doping, the pseudo-gap near $(\pi/2,\pi/2)$ is apparent. In this case there is antiferromagnetic long-range order, but even if we use CPT that does not exhibit long-range order, there appears a pseudogap in that region [123]. The main difference between CPT and VCPT results is the bending back of the bands (for example around the symmetry axis at $(\pi/2,\pi/2)$) caused by halving of the size of the Brillouin zone in the antiferromagnetic case. Form factors [90] are such that the intensity is not symmetric even if the dispersion is. The faint band located at an energy about *t* below the Fermi energy near $(\pi/2,\pi/2)$ was also found in Ref. 89 by a one-loop spin-wave calculation around the Har-tree−Fock antiferromagnetic ground state at $U = 8t$. Experimentalists [86] have suggested the existence of these states. The VCPT results go well beyond the spin-wave calculation (dashed lines in Fig. 40) since one can also see numerous features in addition to remnants of the localized atomic levels around $+5t$ and $-10t$.

The optimally doped case is the real challenge for strong-coupling calculations. The spin-wave approach in Ref. 89 never shows the weight near $(\pi/2,\pi/2)$ that is seen in experiment (Fig. 41). Early mean-field calculations by Kusko et al. [90] suggest that this $(\pi/2,\pi/2)$ feature appears for $U = 3t$. This is very small compared with U of the order of the bandwidth $8t$ necessary to have a Mott insulator at half-filling. We already discussed in Sec. 3.1 that both CPT and TPSC show that weight near $(\pi/2,\pi/2)$ appears for U not too large, say of order $6t$. This same result is also obtained in the Kotliar-Ruckenstein slave boson ap-proach [88].

Since TPSC is valid for a system of infinite size, we present detailed comparisons [87] with experiment

Fig. 42. EDC $A_<(\mathbf{k},\omega) \equiv A(\mathbf{k},\omega)f(\omega)$ along the Fermi sur-face calculated in TPSC (left column) at optimal doping for $t' = -0.175t$, $t'' = 0.05t$, $t = 350$ meV and corresponding ARPES data on NCCO (right column). From Ref. 87.

[86] on $Nd_{1.85}Ce_{0.15}CuO_4$, an electron-doped cu-prate. We take $t' = -0.175t$, $t'' = 0.05t$. Results obtained with $t' = -0.275$ are very close to those we present. With the values used in CPT, $t' = -0.3t$, $t' = 0.2t$, $U = 6t$, TPSC does not lead to strong enough anti-ferromagnetic fluctuations to obtain non-trivial ef-fects in the temperature range studied, $\beta = 20t$. We take $t = 350$ meV. Fig. 39 shows the correspondence between EDC and MDC. Comparisons with experi-mental EDC at wave vectors along the non-interact-ing Fermi surface appear in Fig. 42 for $U = 5.75t$ and 15 doping ($n = 1.15$). The dashed lines indicate the quite detailed agreement between theory and experi-ment. At the hot spot, (middle dashed line), the

Fig. 43. EDC $A_<(\mathbf{k},\omega) \equiv A(\mathbf{k},\omega)f(\omega)$ along two other di-rections calculated for $t' = -0.175t$, $t'' = 0.05t$, $t = 350$ meV in TPSC (left column) and corresponding ARPES data on NCCO (right column). From Ref. 87.
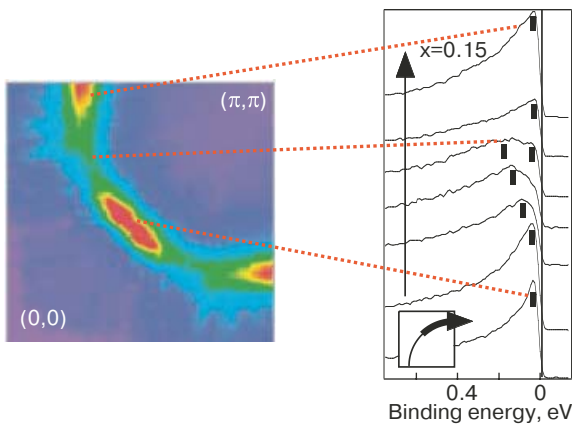

Fig. 41. Experimental Fermi surface plot (MDC at the Fermi energy) for NCCO (left) and corresponding energy distribution curves (right) for 15 electron-doping. From Ref. 86.
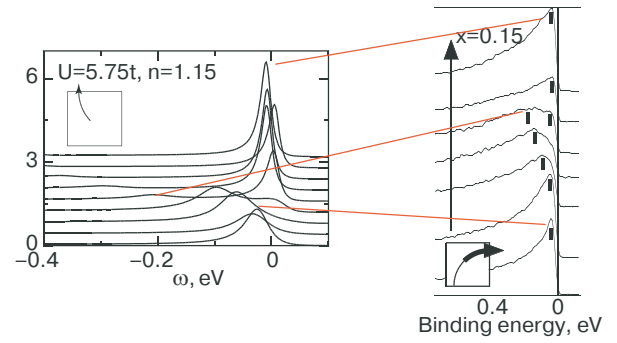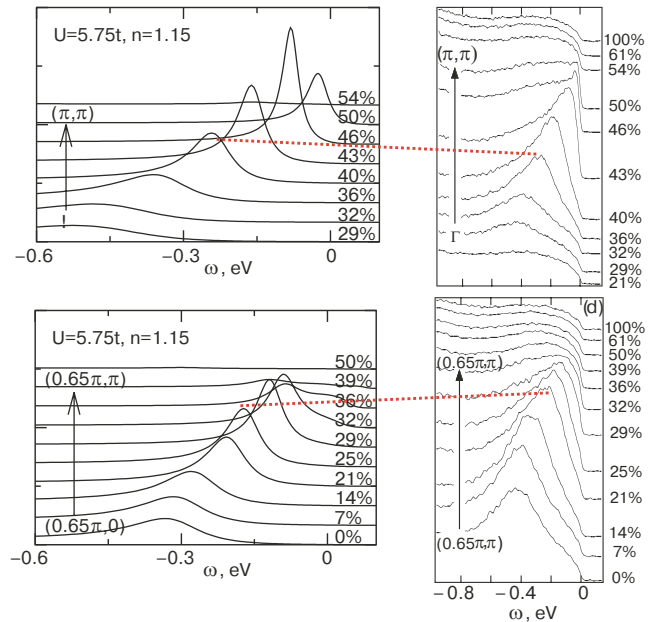
weight is pushed back about 0.2 eV and there is a very small peak left at the Fermi surface, as in the experiment. If U is not large enough the antiferromagnetic fluctuations are not strong enough to lead to a pseudogap. As in CPT (Fig. 21), if U is too large the $(\pi/2, \pi/2)$ weight disappears, as illustrated earlier in Fig. 29. In Fig. 43, cuts along the $(0,0)$ to (π,π) and $(0.65\pi,0)$ to $(0.65\pi,\pi)$ directions are compared with experiment. Again the peak positions and widths are very close, except for some experimental tails extending in the large binding energy direction. The theoretical results have similar asymmetry, but not as pronounced. Experimentally, the large binding energy tails («the background») are the least reproducible features from sample to sample [124]. The experimental renormalized Fermi velocities are $3.31 \cdot 10^5$ m/s and $3.09 \cdot 10^5$ m/s along the zone diagonal and along the $(\pi,0)-(\pi,\pi)$ direction, respectively. The corresponding renormalized Fermi velocities obtained by TPSC are $3.27 \cdot 10^5$ and $2.49 \cdot 10^5$ m/s, respectively. The agreement is very good, particularly along the diagonal direction. The bare Fermi velocities are renormalized in TPSC by roughly a factor of two [125].

As we move towards half-filling, we have to increase U slightly to find agreement with experiment, as discussed earlier in Fig. 29. Figure 44 shows how well the EDC's agree for a Fermi surface cut at 10% doping ($n = 1.10$). The increase is expected physically from the fact that with fewer electrons the contribution to screening that comes from Thomas Fermi physics should not be as good. This is also consistent with the fact that a larger value of U is necessary to explain the Mott insulator at half-filling. It would also be possible to mimic the ARPES spectrum by keeping U fixed and changing the hopping parameters, but the changes would be of order 20%, which does not appear realistic [87].
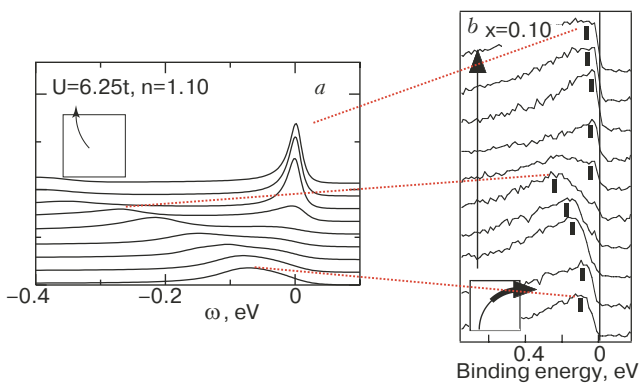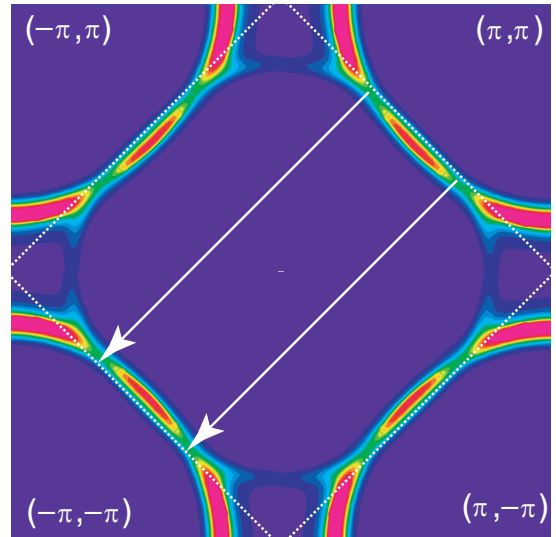

Fig. 45. Hot spots from quasi-static scatterings off antiferromagnetic fluctuations (renormalized classical regime).

We have already explained that the physics behind the pseudogap in TPSC is scattering by nearly critical antiferromagnetic fluctuations. This is illustrated in Fig. 45. If this explanation is correct, the antiferromagnetic correlation length measured by neutron scattering should be quite large. The results of the measurement [126,127] and of the TPSC calculations are shown in Fig. 46. The agreement is again surprisingly good. As we move to smaller dopings $n = 1.1$ (not shown) the agreement becomes less good, but we do expect TPSC to deteriorate as U increases with underdoping. The arrow points to the temperature where EDC's shown earlier were calculated. Note however that the neutron measurements were done on samples that were not reduced, by contrast with the ARPES measurements mentioned earlier. We are expecting experiments on this subject [129]. We should point

Fig. 44. EDC $A_<(\mathbf{k},\omega) \equiv A(\mathbf{k},\omega) f(\omega)$ along the Fermi surface shown for $n = 1.10$, $U = 6.25t$ (*a*) and corresponding energy distribution curves (*b*). Lines are shifted by a constant for clarity. From Ref. 87.
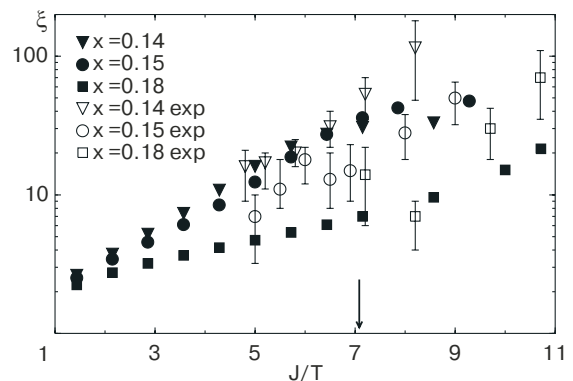

Fig. 46. Semi-log plot of the AFM correlation length (in units of the lattice constant) against inverse temperature (in units of $J = 125$ meV). Filled symbols denote calculated results and empty ones experimental data of Ref. 126 and Ref. 127 ($x = 0.15$). From Ref. 87.
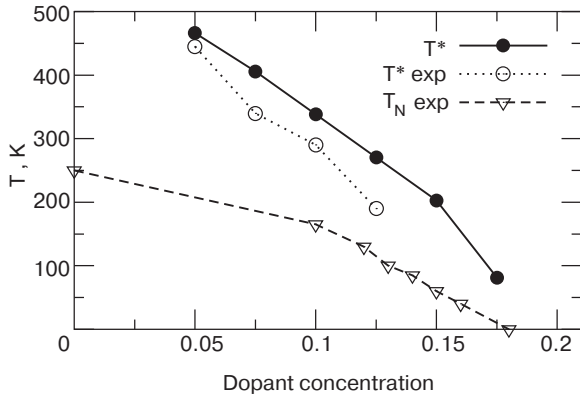
Fig. 47. Pseudogap temperature T^* (filled circles denote T^* calculated from TPSC, empty ones experimental data extracted from optical conductivity [128]). Empty triangles are experimental Néel temperatures T_N. The samples are reduced [126]. From Ref. 87.

out that the EDC's depend strongly on temperature and on the actual value of the antiferromagnetic correlation length only in the vicinity of the temperature where there is a crossover to the pseudogap regime. Decreasing the temperature makes the $\omega = 0$ peaks near $(\pi, 0)$ sharper [87] as observed experimentally [130].

The ARPES pseudogap temperature T^* has been predicted with TPSC [87]. The predictions are shown by the solid line in Fig. 47. The pseudogap temperature observed in optical experiments [128] is shown by the open circles. It differs from the ARPES result, especially as we move towards optimal doping. The size of the pseudogap observed in the optical experiments [128] ($10T^*$) is comparable to the ARPES pseudogap. The solid line in Fig. 47 contains several predictions. If we look at 13% doping ($n = 1.13$), the line predicts $T^* \sim 250$ K. Experiments that were done without being aware of this prediction [131] have verified it. It would be most interesting to do neutron scattering experiments on the same samples to check whether the antiferromagnetic correlation length ξ and the thermal de Broglie wave length ξ_{th} are comparable at that temperature, as predicted by TPSC. Fig. 47 also predicts that the pseudogap induced by antiferromagnetic fluctuations will disappear at the quantum critical point where long-range antiferromagnetic order disappears, in other words it will coincide with the crossing of the experimentally observed Néel temperature (dashed line with triangles in Fig. 47) with the zero temperature axis (if that crossing is not masked by the superconducting transition). Recent optical conductivity experiments [132,133] confirm this prediction as well.

In TPSC, superconducting fluctuations can also lead to a pseudogap by an analogous mechanism [22].

4.3. The phase diagram for high-temperature superconductors

The main features appearing in the phase diagram of high-temperature superconductors are the pseudogap phase, the antiferromagnetic phase and the d-wave superconducting phase. Fig. 48 [110] shows the typical diagram with hole doping to the right and electron doping to the left. Zero on the horizontal axis corresponds to half-filling. There are other features on the phase diagram, in particular checkerboard patterns [134] or stripe phases [135] that appear in general close to the region where antiferromagnetism and superconductivity come close to each other. Before we try to understand these more detailed features, one should understand the most important phases. In the previous subsection we have discussed the pseudogap phase, in particular on the electron-doped side (not indicated on Fig. 48). A recent review of the pseudogap appears in Ref. 136. In the following, we discuss in turn the phase diagram and then the nature of the superconducting phase itself and its relation to the Mott phenomenon.

4.3.1. Competition between antiferromagnetism and superconductivity

We have already shown in Fig. 32 the prediction of VCPT for the zero-temperature phase diagram [18]. Here, we just point out how closely the position of the antiferromagnetic phase boundary, appearing in the lower panel, coincides with the experimental phase diagram in Fig. 38. (Note that electron concentration increases from right to left on this experimental phase diagram.) In particular, there is little size dependence to the position of this boundary, (6 to 10 sites) and in addition the dependence on the value of U is also weak, as can be seen from Fig. 34. Hence, the positions of the antiferromagnetic phase boundaries is a
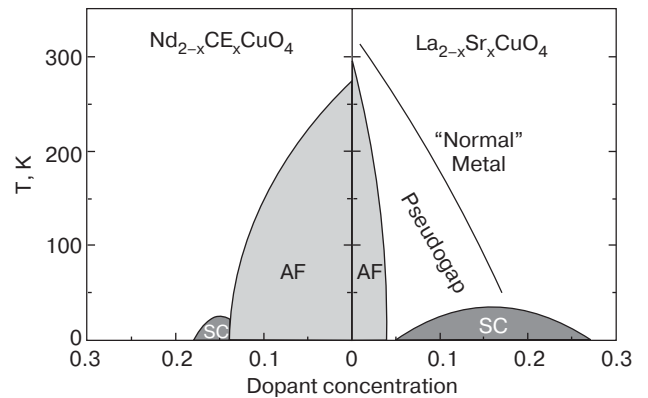

Fig. 48. The generic phase diagram of high-T_C superconductors, from Ref. 110. There should also be a pseudogap line on the electron-doped side. It was not well studied at the time of publication of that paper.
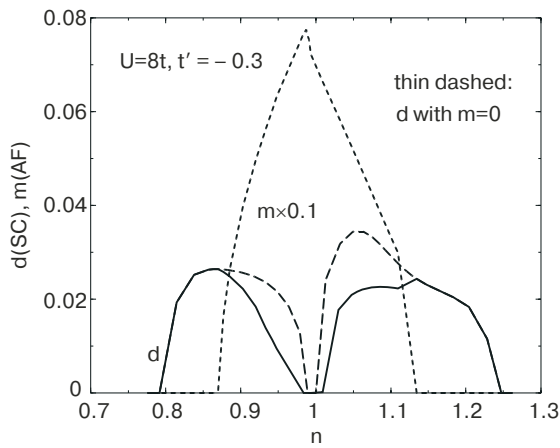
Fig. 49. Antiferromagnetic order parameter m (dashed) and d-wave (solid) order parameter obtained from CDMFT on a 2×2 cluster. The result obtained by forcing $m = 0$ is also shown as a thin dashed line.

robust prediction of VCPT. The CDMFT result for a four site cluster in a bath is shown in Fig. 49 for $t' = -0.3t$, $t'' = 0$ and $U = 8t$. The agreement with experiment is not as good. Despite the useful presence of a bath in CDMFT, the cluster itself is of size 2×2, which is probably smaller than the Cooper pair size.

The d-wave superconducting order parameter on the top panel of Fig. 32 shows more size dependence than the antiferromagnetic order parameter. Nevertheless, there are some clear tendencies: (a) d-wave superconductivity can exist by itself, without antiferromagnetism. The vertical lines indicate the location of the end of the antiferromagnetic phase for the various system sizes to help this observation. (b) The range where d-wave-superconductivity exists without antiferromagnetism, is about three times larger on the hole than on the electron-doped side, as observed experimentally. (c) As system size increases, the maximum d-wave order parameter is larger on the hole than on the electron-doped side. (d) The tendency to have coexisting antiferromagnetism and d-wave superconductivity is rather strong on the electron-doped side of the phase diagram. This is observed experimentally [137] but only over a rather narrow region near optimal doping. Recent experiments [138] challenge this result, others [139,140] indicate that antiferromagnetism can be induced from the d-wave superconducting phases with very small fields. (e) On the hole-doped side, d-wave superconductivity and antiferromagnetism coexist for a very narrow range of dopings for system size $N_c = 6$, for a broad range extending to half-filling for $N_c = 8$ and not at all for $N_c = 10$. In other words, the tendency to coexistence is not even monotonic. We interpret this result as a reflection of the tendency to form stripes observed experimentally on the hole-doped side [135,141,142].
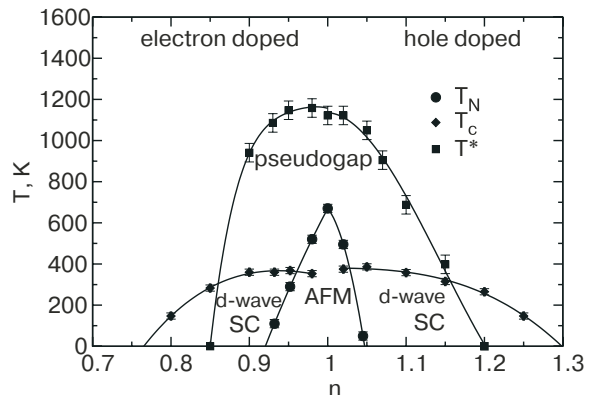

Fig. 50. Phase diagram obtained from DCA for $U = 8t$ for the two-band model. From Ref. 104.

We cannot study systems large enough to allow for striped inhomogeneous states to check this statement.

The more realistic two-band model has also been studied using DCA [104]. The results are shown on Fig. 50. Electron concentration increases from right to left. This phase diagram is very close to that obtained with the same method from the one-band Hubbard model [104] with $t' = -0.3t$, $t'' = 0$, $U = 8t$. The qualitative results agree with the other calculations and with experiment: antiferromagnetism extends over a narrower doping range for hole than for electron doping and d-wave superconductivity by itself exists over a broader range for the hole-doped case than for the electron-doped case. The actual ranges where antiferromagnetism and d-wave superconductivity exist are not in as good an agreement with experiment as in the VCPT case. However, as in CDMFT, the system sizes, 2×2, are very small. Overall then, quantum cluster methods, VCPT in particular, allow us to obtain from the Hubbard model the two main phases, antiferromagnetic and d-wave superconducting, essentially in the observed doping range of the zero-temperature phase diagram. At finite temperature, DCA and TPSC agree on the value of T_c for the particle-hole symmetric model at 10% doping and $U = 4t$. Recent studies of the irreducible vertex using DCA [143] also show that in the weak-coupling limit the particle-particle d-wave channel leads to an instability driven by antiferromagnetic fluctuations as temperature decreases, as found in TPSC.

To understand the effect of pressure on the phase diagram, note that U/t should decrease as pressure increases since the increase in the overlap between orbitals should lead mainly to an increase in t. Hence, as can be deduced from Fig. 37, applying pressure should lead to a decrease in the value of T_c at weak coupling, concomitant with the decrease in antiferromagnetic fluctuations that lead to pairing in the weak coupling case. This is indeed what pressure does experimentally in the case of electron-doped high-

temperature superconductors [144], reinforcing our argument that near optimal doping they are more weakly coupled. It is widely known on the other hand that pressure *increases* T_c in hole-doped systems. That is consistent with the strong-coupling result that we found in VCPT and CDMFT, namely that the maximum d-wave order parameter in that case scales with $J = 4t^2/U$, a quantity that increases with t and hence pressure. Whereas in the weak coupling case superconductivity is a secondary phenomenon that occurs after antiferromagnetic fluctuations have built up, in strong coupling they can be two distinct phenomena as can be seen from the phase diagram, even though they arise from the same microscopic exchange interaction represented by J.

4.3.2. Anomalous superconductivity near the Mott transition

Superconductivity in the underdoped regime is very much non-BCS. First of all, we notice in Fig. 35 obtained in CDMFT [16] that at strong coupling the d-wave superconducting order parameter vanishes as we move towards half-filling even in the absence of long-range antiferromagnetic order. In other words, the Mott phenomenon by itself suffices to destroy d-wave superconductivity. This conclusion is reinforced by the fact that at weak coupling $(U = 4t)$ where there is no Mott localization, d-wave superconductivity survives at half-filling. In the presence of antiferromagnetic long-range order, that last statement would not be true, as confirmed by VCPT calculations in Fig. 36: at $U = 4t$ d-wave superconductivity survives at half-filling if we do not allow for antiferromagnetic long-range order but it disappears if we do. In BCS theory, the presence of an interaction J that leads to attraction in the d-wave channel would lead at $T = 0$ to d-wave superconductivity at all dopings including half-filling, unless we allow for competing long-range order. At strong coupling, no long-range order is necessary to destroy d-wave superconductivity.

Superconductivity at strong coupling [145,146] also differs from BCS in the origin of the condensation energy. Suppose we do BCS theory on the attractive Hubbard model. Then, as in the usual BCS model, kinetic energy is increased in the superconducting state because the Fermi surface is no-longer sharp. On the other hand, in the superconducting phase there is a gain in potential energy. The reverse is true at strong coupling, as demonstrated in Fig. 51 obtained from CDMFT [16]. This result also follows from DCA [121] and is in agreement with the kinetic energy drop in the superconducting state that has been estimated from the f-sum rule in optical conductivity experi-
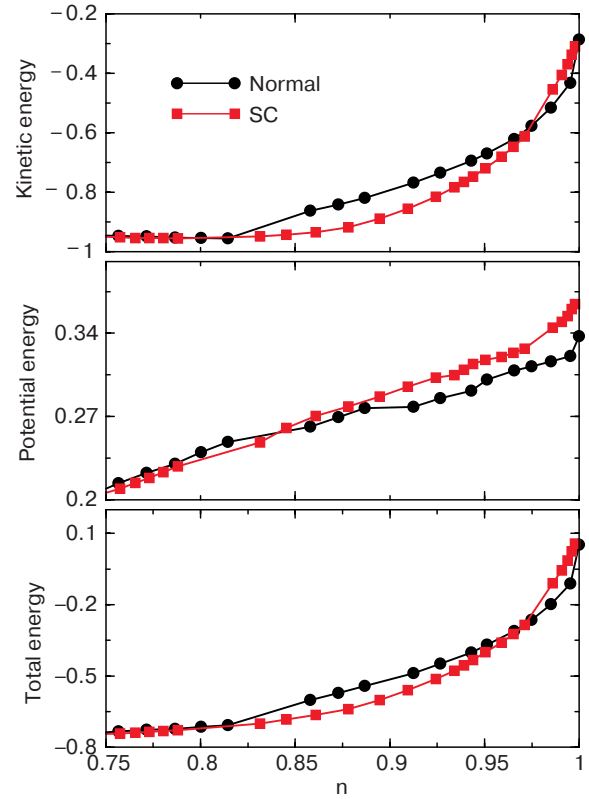
Fig. 51. Kinetic, potential and total energies of the normal and dSC states for $U = 8t$, $t' = 0$ as calculated in CDMFT on a 2×2 cluster. From Ref. 16.

ments [147−149]. Photoemission data [145] had also suggested this kinetic energy drop in the superconducting state. A crossover from non-BCS-like to BCS behavior in the condensation mechanism as we go from underdoping to overdoping has also been seen recently experimentally [147]. We do not seem to have the resolution to find that crossover since the condensation energy becomes very small on the overdoped side. We expect that crossover from strong to weak coupling will also lead to a change from a kinetic-energy driven
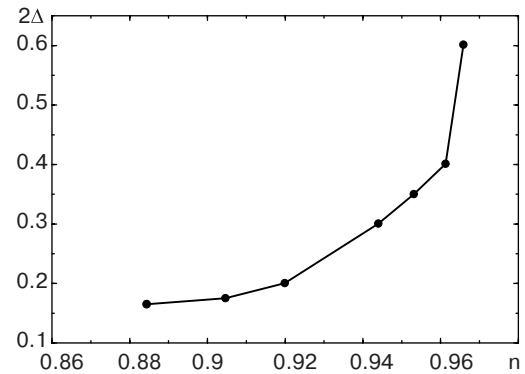

Fig. 52. The dSC gap as a function of filling for $U = 8t$, $t' = -0.3t$ as calculated in CDMFT on a 2×2 cluster. From Ref. 16.

to a potential-energy driven pairing mechanism. This is confirmed by CDMFT calculations for the attractive Hubbard model [151].

A third way in which superconductivity in the underdoped regime is non-BCS is that the drop in the order parameter as we go towards half-filling is accompanied by an increase in the d-wave gap as measured in the single-particle density of states. Figure 6 of Ref. 152 summarizes the experimental evidence for the increase in the size of the *d*-wave gap. That increase, observed in the CDMFT calculation of the *d*-wave gap, is illustrated in Fig. 52 [16].

5. Conclusion, open problems

High-temperature superconductivity has forced both experimentalists and theorists to refine their tools and to develop new ones to solve the puzzles offered by this remarkable phenomenon. From a theoretical perspective, the original suggestion of Anderson [1] that the physics was in the one-band Hubbard model is being confirmed. In the absence of *ab initio* methods to tell us what is the correct starting point, such insight is essential. The non-perturbative nature of the phenomenon has however forced theorists to be extremely critical of each other's theories since none of them can pretend that a small parameter controls the accuracy of the approximations.

If theorists are to convince each other and experimentalists that a solution of the high-temperature superconductivity problem has been found, then the theories have to give quantitative results and to make predictions. Unlike most traditional problems in condensed matter physics however, the non-perturbative nature of the problem means that no simple mean-field like theory can be trusted, even if it seems to agree qualitatively with experiment. In fact several such theories have been proposed [12,13,153] not long after the experimental discovery of the phenomenon but they have not been accepted immediately. Theories have to be internally consistent, they have to agree with exact results whenever they are available, and then they can be compared with experiments. If there is a disagreement with experiment, the starting point (one-band Hubbard model) needs to be reconsidered. When approaches developed on the basis of weak-coupling ideas agree at intermediate coupling with approaches developed on the basis of strong-coupling ideas, then one gains confidence in the validity of the results. We have argued that such concordance is now found in a number of cases and that corresponding rather detailed quantitative agreement with experiment can be found. In a non-perturbative context it becomes essential to also cross check various approaches.

The main theoretical methods that we have discussed are those that we have developed or perfected or simply used in our group: the two-particle self-consistent approach that is based on weak-coupling but non-perturbative ideas (no diagrams are involved), as well as heavily numerical approaches such as QMC and various quantum cluster methods, VCPT and CDMFT.

Based on our own work and that of many others, we think the following experimental facts about high-temperature superconductivity can be reproduced very accurately by calculations for the one-band Hubbard model with U in the intermediate coupling range ($U \sim 8t$) with $t \sim 350$ meV, and hopping parameters t' and t'' close to the values suggested by band structure calculations [103], namely $t' = -0.3t$, $t'' = 0.2t$.

(i) In the one-band Hubbard model the main phases of the zero-temperature phase diagram, namely antiferromagnetic and *d*-wave superconducting, appear very near the observed ranges for both the hole- and electron-doped cases.

(ii) The normal state is unstable to a *d*-wave superconducting phase in a temperature range that has the correct order of magnitude. As usual the value of T_c is the most difficult quantity to evaluate since one must take into account Kosterlitz–Thouless physics as well as the effect of higher dimensions etc, so this level of agreement must be considered satisfying.

(iii) The ARPES MDC at the Fermi energy and the EDC near the Fermi energy are qualitatively well explained by cluster calculations for both hole- and electron-doped cases. These comparisons, made at a resolution of about 30 to 60 meV are not very sensitive to long-range order, although order does influence the results. One is mainly sensitive to the pseudogap, so this is the main phenomenon that comes out from the model. Energy resolution is not good enough to see a kink. More details about what aspects of ARPES are understood may be found in Sec. 4.1.

(iv) In the case of electron-doped cuprates, the value of U near optimal doping seems to be in the range $U \sim 6t$, which means that it is accessible to studies with TPSC that have better resolution. In that case, the agreement with experiment is very accurate, even if there is room for improvement. In addition, the value of T^* for 13% doping has been predicted theoretically before it was observed experimentally, one of the very rare predictions in the field of high-temperature superconductors. All of this agreement with ARPES data is strong indication that $U \sim 6t$ is appropriate to describe electron-doped superconductors near optimal doping. Additional arguments come from the pressure dependence of the superconducting tran-

sition temperature T_c, which increases with t/U contrary to the strong-coupling result, and from simple ideas on Thomas−Fermi screening. The latter would predict that the screened interaction scales like $\partial\mu/\partial n$ and CPT results do lead to $\partial\mu/\partial n$ smaller on the electron- than on the hole-doped side [77].

What is the physics? The physics of the antiferromagnetic phase at both weak and strong coupling is well understood and needs no further comment. For the pseudogap, we have argued that there seems to be two mechanisms, a weak coupling one that involves scattering off critical fluctuations and that is very well understood within TPSC, and a strong-coupling one where there is no need for large correlation lengths. There is no simple physical picture for the latter mechanism although the fact that it does not scale with J but with t seems to suggest forbidden hopping. The pseudogap is clearly different from the Mott gap. Whether there is a phase transition as a function of U that separates the weak and strong coupling regimes or whether there is only a crossover is an open question. The shape of the MDC's at the Fermi energy clearly show in any case that in some directions wave vector is not such a bad quantum number whereas in the pseudogap direction, a «localized» or «almost localized» particle-like picture would be appropriate. In fact the pseudogap occurs near the intersection with the antiferromagnetic zone boundary that turns out to also be the place where umklapp processes are possible. In other words, the presence of a lattice is extremely important for the appearance of the pseudogap. We have seen that with spherical Fermi surfaces the Fermi liquid survives even for large U. The dichotomy between the wave description inherent to the Fermi liquid and the particle (localized) description inherent to the Mott phenomenon seems to be resolved in the pseudogap phase by having certain directions where electrons are more wave-like and other directions where particle-like (gapped) behavior appears. The latter behavior appears near regions where the presence of the lattice is felt through umklapp processes.

It is clear that when weak-coupling-like ideas of quasiparticles scattering off each other and off collective excitations do not apply, a simple physical description becomes difficult. In fact, knowing the exact wave functions would give us the solution but we would not know how to understand «physically» the results.

This lack of simple physical images and the necessity to develop a new discourse is quite apparent for d-wave superconductivity. At weak coupling exchange of slow antiferromagnetic fluctuations is at the origin of the phenomenon, while at strong-coupling

the fact that the maximum value of the d-wave order parameter scales with J tells us that this microscopic coupling is important, even though there is no apparent boson exchange. This is where mean-field like theories [12,13,153] or variational approaches [4] can help when they turn out to give results that are confirmed by more accurate and less biased methods.

There are many open problems, some of which are material dependent and hence may depend on interactions not included in the simplest Hubbard model. We have already mentioned the problem of the chemical potential shift in ARPES for very small dopings [117] that seems to be somewhat material dependent [118]. It would also be important to understand additional inhomogeneous phases that are observed in certain high-temperature superconductors. That is extremely challenging for quantum cluster methods and unlikely to be possible in the very near future, except for inhomogeneities of very short wave length. Also, we still need to improve concordance between the methods before we can make predictions that are quantitative at the few percent level for all physical quantities. Apart from DCA, there are no quantum cluster methods that have been developed yet to study two-particle response functions that are necessary to obtain results on the superfluid density and on transport in general. Transport studies are being completed in TPSC [154]. Such studies are crucial since they are needed to answer questions such as: (i) Why is it that for transport properties, such as optical conductivity, the number of carriers appears to scale with doping whereas in ARPES the surface of the Brillouin zone enclosed by the apparent Fermi surface appears to scale with the number of electrons? Is it because the weight of quasiparticles at the Fermi surface scales like the doping or because of vertex corrections or because of both? (ii) Can we explain a vanishing superfluid density as doping goes to zero [155] only through Mott physics or can competing order do the job [156,99].

After twenty years all the problems are not solved, but we think that we can say with confidence that the essential physics of the problem of high-temperature superconductivity is in the one-band Hubbard model. At least the pseudogap, the antiferromagnetic and the d-wave superconducting phases come out from the model. Refinements of that model may however be necessary as we understand more and more details of the material-specific experimental results.

Has a revolution been necessary to understand the basic physics of high-temperature superconductors? Certainly, it has been necessary to change our attitude towards methods of solution. We have seen that to study intermediate coupling, even starting from weak

coupling, it has been necessary to drop diagrams and to rely instead on sum rules and other exact results to devise a non-perturbative approach. At strong coupling we had to accept that numerical methods are essential for progress and that we need to abandon some of the traditional physical explanations of the phenomena in terms of elementary excitations. Even though progress has been relatively slow, the pace is accelerating in the last few years and there is hope that in a few years the problem will be considered for the most part solved. The theoretical methods (numerical and analytical) that have been developed and that still need to be developed will likely remain in the tool box of the theoretical physicist and will probably be useful to understand and perhaps even design other yet undiscovered materials with interesting properties. The success will have been the result of the patient and focused effort of a large community of scientists fascinated by the remarkable phenomenon of high-temperature superconductivity.

Acknowledgments

Appendix: List of acronyms

ARPES: angle resolved photoemission spectroscopy: experiment from which one can extract $A(\mathbf{k}, \omega) f(\omega)$.

CPT: cluster perturbation theory: cluster method based on strong coupling perturbation theory [53,54,62].

CDMFT: cellular dynamical mean field theory: a cluster generalization of DMFT that allows one to take into account both wave vector and frequency dependence of the self-energy [58]. It is best formulated in real space.

DCA: dynamical cluster approximation: a cluster generalization of DMFT that allows one to take into account both wave vector and frequency dependence of the self-energy based on coarse graining of the self-energy in reciprocal space [55,157].

DMFT: dynamical mean field theory: this approach is exact in infinite dimension. It takes the frequency dependence of the self-energy into account and includes both the Mott and the Fermi liquid limits [2,3].

EDC: energy dispersion curves: a representation of $A(\mathbf{k}, \omega) f(\omega)$ at fixed $\mathbf{k}$ as a function of ω.

FLEX: fluctuation exchange approximation: a conserving many-body approach, similar in spirit to eliashberg theory [21].

MDC: momentum dispersion curves: a representation of $A(\mathbf{k}, \omega) f(\omega)$ at fixed ω as a function of $\mathbf{k}$.

QMC: quantum Monte Carlo: determinental approach [158]. This provides an essentially exact solution to the model for a given system size and within statistical errors that can be made smaller by performing more measurements.

RPA: random phase approximation.

TPSC: two-particle self-consistent approach: based on sum rules and other constraints, allows to treat the Hubbard model non-perturbatively in the weak to intermediate coupling limit [22,34].

VCA: variational cluster approach. Analogous to CDMFT but with a convergence criterion based on an extremum principle. In the applications quoted here, there is no bath [56,64,73,159].

VCPT: variational cluster perturbation theory. In the present paper synonymous with VCA.

1. P. Anderson, *Science* **235**, 1196 (1987).
2. A. Georges, G. Kotliar, W. Krauth, and M. Rozenberg, *Rev. Mod. Phys.* **68**, 13 (1996).
3. M. Jarrell, *Phys. Rev. Lett.* **69**, 168 (1992).
4. A. Paramekanti, M. Randeria, and N. Trivedi, *Phys. Rev.* **B70**, 54504 (2004).
5. M. Beal-Monod, C. Bourbonnais, and V. Emery, *Phys. Rev.* **B34**, 7716 (1986).
6. K. Miyake, S. Schmitt-Rink, and C. Varma, *Phys. Rev.* **B34**, 6554 (1986).
7. D. Scalapino, E. Loh, and J. Hirsch, *Phys. Rev.* **B34**, 8190 (1986).
8. W. Kohn and J.M. Luttinger, *Phys. Rev. Lett.* **15**, 524 (1965).
9. A. Leggett, *Rev. Mod. Phys.* **47**, 331 (1975).
10. J. Hirsch and H. Lin, *Phys. Rev.* **B37**, 5070 (1988).
11. S. Zhang, J. Carlson, and J.E. Gubernatis, *Phys. Rev. Lett.* **78**, 4486 (1997).
12. M. Inui, S. Doniach, P. Hirschfeld, and A. Ruckenstein, *Phys. Rev.* **B37**, 2320 (1988).
13. G. Kotliar and J. Liu, *Phys. Rev. Lett.* **61**, 1784 (1988).

14. T. Maier, M. Jarrell, T. Pruschke, and J. Keller, *Phys. Rev. Lett.* **85**, 1524 (2000).

15. D. Poilblanc and D. Scalapino, *Phys. Rev.* **B66**, 052513 (2002).

16. S.S. Kancharla, M. Civelli, M. Capone, B. Kyung, D. Sénéchal, G. Kotliar, and A.-M. Tremblay, *Anomalous Superconductivity in Doped Mott Insulators* (2005), *cond-mat/0508205*.

17. T. Maier, M. Jarrell, T. Schulthess, P. Kent, and J. White, *A Systematic Study of Superconductivity in the 2D Hubbard Model* (2005), *cond-mat/0504529*.

18. D. Sénéchal, P.-L. Lavertu, M.-A. Marois, and A.-M.S. Tremblay, *Phys. Rev. Lett.* **94**, 156404 (2005).

19. T. Moriya, *Spin Fluctuations in Itinerant Electron Magnetism*, Springer-Verlag (1985).

20. R.S. Markiewicz, *Phys. Rev.* **B70**, 174518 (2004).

21. N. Bickers and D. Scalapino, *Ann. Phys. (USA)* **193**, 206 (1989).

22. Y. Vilk and A.-M. Tremblay, *J. Phys I (France)* **7**, 1309 (1997).

23. Y. Vilk and A.-M. Tremblay, *Europhys. Lett.* **33**, 159 (1996).

24. N. Furukawa, T.M. Rice, and M. Salmhofer, *Phys. Rev. Lett.* **81**, 3195 (1998).

25. C. Halboth and W. Metzner, *Phys. Rev.* **B61**, 7364 (2000).

26. V. Hankevych and F. Wegner, *Eur. Phys. J.* **B31**, 333 (2003).

27. C. Honerkamp and M. Salmhofer, *Phys. Rev. Lett.* **87**, 187004 (2001).

28. F. Wegner and V. Hankevych, *Acta Phys. Pol.* **B34**, 497 (2003).

29. A.A. Katanin and A.P. Kampf, *Phys. Rev. Lett.* **93**, 106406 (2004).

30. D. Zanchi, *Europhys. Lett.* **55**, 376 (2001).

31. Y. Vilk and A.-M. Tremblay, *J. Phys. Chem. Solids (UK)* **56**, 1769 (1995).

32. Y. Vilk, L. Chen and A.-M. Tremblay, *Phys. Rev.* **B49**, 13267 (1994).

33. G. Mahan, *Many-Particle Physics, 3rd Edition*, Section 6.4.4 -Kluwer/Plenum (2000).

34. S. Allen, A.-M. Tremblay, and Y.M. Vilk, in: *Theoretical Methods for Strongly Correlated Electrons*, D. Sénéchal, C. Bourbonnais, and A.-M. Tremblay (eds.), *CRM Series in Mathematical Physics*, Springer (2003).

35. G. Baym, *Phys. Rev.* **127**, 1391 (1962).

36. S. Moukouri, S. Allen, F. Lemay, B. Kyung, D. Poulin, Y. Vilk, and A.-M. Tremblay, *Phys. Rev.* **B61**, 7887 (2000).

37. This additional constraint leads to a degree of consistency between one- and two-particle quantities that is absent from the standard Hartree−Fock factorization.

38. The constant self-energy is *not* equal to $Un_{-\sigma}$ as it would in the trivial Hartree−Fock factorization (see previous note).

39. S. Roy, C. Brillon, and A.-M. Tremblay, *unpublished*.

40. S. Allen, B. Kyung, and A.-M. Tremblay, *unpublished*.

41. B. Kyung, J.-S. Landry, and A.M.S. Tremblay, *Phys. Rev.* **B68**, 174502 (2003).

42. L. Lilly, A. Muramatsu, and W. Hanke, *Phys. Rev. Lett.* **65**, 1379 (1990).

43. S. Allen and A.-M. Tremblay, *Phys. Rev.* **B64**, 075115 (2001).

44. B. Kyung, S. Allen, and A.-M. Tremblay, *Phys. Rev.* **B64**, 075116 (2001).

45. A. Daré, Y. Vilk, and A.-M. Tremblay, *Phys. Rev.* **B53**, 14236 (1996).

46. S. White, D.J. Scalapino, and R. Sugar, *Phys. Rev.* **B39**, 839 (1989).

47. L. Chen, C. Bourbonnais, T. Li, and A.-M.-S. Tremblay, *Phys. Rev. Lett.* **66**, 369 (1991).

48. N. Bulut, D. Scalapino, and S. White, *Phys. Rev.* **B47**, 2742 (1993).

49. V. Hankevych, B. Kyung, and A.-M. Tremblay, *Phys. Rev.* **B68**, 214405 (2003).

50. A. Georges and G. Kotliar, *Phys. Rev.* **B45**, 6479 (1992).

51. N. Trivedi and M. Randeria, *Phys. Rev. Lett.* **75**, 312 (1995).

52. A. Moreo, D.J. Scalapino, and S.R. White, *Phys. Rev.* **B45**, 7544 (1992).

53. C. Gros and R. Valenti, *Phys. Rev.* **B48**, 418 (1993).

54. D. Sénéchal, D. Perez, and M. Pioro-Ladriere, *Phys. Rev. Lett.* **84**, 522 (2000).

55. M.H. Hettler, A.N. Tahvildar-Zadeh, M. Jarrell, T. Pruschke, and H. Krishnamurthy, *Phys. Rev.* **B58**, R7475 (1998).

56. M. Potthoff, *Eur. Phys. J.* **B36**, 335 (2003).

57. M. Potthoff, M. Aichhorn, and C. Dahnken, *Phys. Rev. Lett.* **91**, 206402 (2003).

58. G. Kotliar, S. Savrasov, G. Pálsson, and G. Biroli, *Phys. Rev. Lett.* **87**, 186401 (2001).

59. T. Stanescu and G. Kotliar, *Cluster Dynamical Mean Field Theories: A Strong Coupling Perspective* (2005), *cond-mat/0508302*.

60. T.D. Stanescu and G. Kotliar, *Phys. Rev.* **B70**, 205112 (2004).

61. T. Maier, M. Jarrell, T. Pruschke, and M.H. Hettler, *Rev. Mod. Phys.* **77**, 1027 (2005).

62. D. Sénéchal, D. Perez, and D. Plouffe, *Phys. Rev.* **B66**, 075129 (2002).

63. M. Potthoff, *Non-Perturbative Construction of the Luttinger-Ward Functional* (2004), *cond-mat/0406671*.

64. M. Potthoff, *Dynamical Variational Principles for Strongly Correlated Electron Systems* (2005), *cond-mat/0503715*.

65. M. Caffarel and W. Krauth, *Phys. Rev. Lett.* **72**, 1545 (1994).

66. C.J. Bolech, S.S. Kancharla, and G. Kotliar, *Phys. Rev.* **B67**, 075110 (2003).

67. B. Kyung, S. Kancharla, D. Sénéchal, A.M.S. Tremblay, M. Civelli, and G. Kotliar, *Short-Range Correlation Induced Pseudogap in Doped Mott Insulators* (2005), *cond-mat/0502565*.

68. D. Sénéchal, in: *High Performance Computing Systems and Applications and OSCAR Symposium*, D. Sénéchal (ed.) (2003).

69. K. Aryanpour, T.A. Maier, and M. Jarrell, *Phys. Rev.* **B71**, 037101 (2005).

70. G. Biroli and G. Kotliar, *Phys. Rev.* **B65**, 155112 (2002).

71. G. Biroli and G. Kotliar, *Phys. Rev.* **B71**, 037102 (2005).

72. J. Favand, S. Haas, K. Penc, F. Mila, and E. Dagotto, *Phys. Rev.* **B55**, R4859 (1997).

73. C. Dahnken, M. Aichhorn, W. Hanke, E. Arrigoni, and M. Potthoff, *Phys. Rev.* **B70**, 245110 (2004).

74. M. Capone, M. Civelli, S.S. Kancharla, C. Castellani, and G. Kotliar, *Phys. Rev.* **B69**, 195105 (2004).

75. T.A. Maier, O. Gonzalez, M. Jarrell, and T. Schulthess, *Two Quantum Cluster Approximations* (2002), *cond-mat/0205460*.

76. K. Pozgajcic, *Quantitative Aspects of the Dynamical Impurity Approach* (2004), *cond-mat/0407172*.

77. D. Sénéchal and A.-M.S. Tremblay, *Phys. Rev. Lett.* **92**, 126401 (2004).

78. C. Huscroft, M. Jarrell, T. Maier, S. Moukouri, and A. Tahvildarzadeh, *Phys. Rev. Lett.* **86**, 139 (2001).

79. C. Grober, R. Eder, and W. Hanke, *Phys. Rev.* **B62**, 4336 (2000).

80. A. Moreo, S. Haas, A. Sandvik, and E. Dagotto, *Phys. Rev.* **B51**, 12045 (1995).

81. S. Moukouri and M. Jarrell, *Phys. Rev. Lett.* **87**, 167010 (2001).

82. A. Brooks Harris, and Robert V. Lange, *Phys. Rev.* **157**, 295 (1967).

83. M.B.J. Meinders, G.A. Sawatzky, and G.A. Sawatzky, *Phys. Rev.* **B48**, 3916 (1993).

84. B. Kyung, J. Landry, D. Poulin, and A.-M.S. Tremblay, *Phys. Rev. Lett.* **90**, 099702 (2003).

85. F. Ronning et al., *Phys. Rev.* **B67**, 165101 (2003).

86. N. Armitage et al., *Phys. Rev. Lett.* **88**, 257001 (2002).

87. B. Kyung, V. Hankevych, A.-M. Daré, and A.-M.S. Tremblay, *Phys. Rev. Lett.* **93**, 147004 (2004).

88. Q. Yuan, F. Yuan, and C.S. Ting, *Doping Dependence of the Electron-Doped Cuprate Superconductors from the Antiferromagnetic Properties of the Hubbard Model* (2005), *cond-mat/0503056*.

89. H. Kusunose and T.M. Rice, *Phys. Rev. Lett.* **91**, 186407 (2003).

90. C. Kusko, R.S. Markiewicz, M. Lindroos, and A. Bansil, *Phys. Rev.* **B66**, 140513 (2002).

91. K. Borejsza and N. Dupuis, *Phys. Rev.* **B69**, 085119 (2004).

92. J. Carbotte, E. Schachinger, and D. Basov, *Nature* **401**, 354 (1999).

93. D. Scalapino, *Phys. Rep.* **250**, 329 (1995).

94. A. Moreo and D.J. Scalapino, *Phys. Rev.* **B43**, 8211 (1991).

95. R. Scalettar and R. Singh, *Phys. Rev. Lett.* **67**, 370 (1991).

96. A. Paramekanti, M. Randeria, and N. Trivedi, *Phys. Rev. Lett.* **87**, 217002 (2001).

97. S. Sorella, G.B. Martins, F. Becca, C. Gazza, L. Capriotti, A. Parola, and E. Dagotto, *Phys. Rev. Lett.* **88**, 117002 (2002).

98. W. Hanke, M. Aichhorn, E. Arrigoni, and M. Potthoff, *Correlated Band Structure and the Ground-State Phase Diagram in High-T_c Cuprates* (2005), *cond-mat/0506364*.

99. B. Tobijaszewska and R. Micnas, *Phys. Status Solidi* **B242**, 468 (2005).

100. C. Pao and N. Bickers, *Phys. Rev.* **B49**, 1586 (1994).

101. J. Deisz, D. Hess, and J. Serene, *Phys. Rev. Lett.* **76**, 1312 (1996).

102. F. Zhang and T.M. Rice, *Phys. Rev.* **B37**, 3759 (1988).

103. O. Andersen, A. Liechtenstein, O. Jepsen, and F. Paulsen, *J. Phys. Chem. Solids* **56**, 1573 (1995).

104. A. Macridin, T.A. Maier, M.S. Jarrell, and G. Sawatzky, *Phys. Rev.* **B71**, 134527 (2005).

105. R. Coldea, S.M. Hayden, G. Aeppli, T.G. Perring, C.D. Frost, T.E. Mason, S.-W. Cheong, and Z. Fisk, *Phys. Rev. Lett.* **86**, 5377 (2001).

106. J.-Y. Delannoy, *Ph. D. Thesis*, École Normale Supérieure de Lyon (2005).

107. J.-Y.P. Delannoy, M.J.P. Gingras, P.C.W. Holdsworth, and A.-M.S. Tremblay, *Phys. Rev.* **B72**, 115114 (2005).

108. L. Raymond, G. Albinet, and A.-M. Tremblay, *cond-mat/0510811*.

109. A.M. Toader, J.P. Goff, M. Roger, N. Shannon, J.R. Stewart, and M. Enderle, *Phys. Rev. Lett.* **94**, 197202 (2005).

110. A. Damascelli, Z. Hussain, and Z.-X. Shen, *Rev. Mod. Phys.* **75**, 473 (2003).

111. A. Damascelli, *Probing the Low-Energy Electronic Structure of Complex Systems by ARPES* (2003), *cond-mat/0307085*.

112. A. Kordyuk and S.V. Borisenko, *ARPES on HTSC: Simplicity vs. Complexity* (2005), *cond-mat/0510218*.

113. P. Preuss, W. Hanke, and W. von der Linden, *Phys. Rev. Lett.* **75**, 1344 (1995).

114. S. Pairault, D. Sénéchal, and A.-M. Tremblay, *Eur. Phys. J.* B (*France*) **16**, 85 (2000).

115. S. Pairault, D. Sénéchal, and A.-M.S. Tremblay, *Phys. Rev. Lett.* **80**, 5389 (1998).

116. R. Gooding, K. Vos, and P. Leung, *Phys. Rev.* **B50**, 12866 (1994).

117. K. Shen, F. Ronning, D. Lu, F. Baumberger, N. Ingle, W. Lee, W. Meevasana, Y. Kohsaka, M. Azuma, M. Takano et al., *Science* **307**, 901 (2005).

118. T. Yoshida, X.J. Zhou, K. Tanaka, W.L. Yang, Z. Hussain, Z.-X. Shen, A. Fujimori, S. Komiya, Y. Ando, H. Eisaki et al., *cond-mat/0510608*.

119. X. Zhou, T. Yoshida, A. Lanzara, P.V. Bogdanov, S.A. Kellar, K.M. Shen, W.L. Yang, F. Ronning, T. Sasagawa, T. Kakeshita et al., *Nature* **423**, 398 (2003).

120. T.A. Maier, M. Jarrell, A. Macridin, and C. Slezak, *Phys. Rev. Lett.* **92**, 027005 (2004).

121. A.D. Gromko, A.V. Fedorov, Y.-D. Chuang, J.D. Koralek, Y. Aiura, Y. Yamaguchi, K. Oka, Y. Ando, and D.S. Dessau, *Phys. Rev.* **B68**, 174520 (2003).

122. N.P. Armitage, D.H. Lu, C. Kim, A. Damascelli, K.M. Shen, F. Ronning, D.L. Feng, P. Bogdanov, X.J. Zhou, W.L. Yang et al., *Phys. Rev.* **B68**, 064517 (2003).

123. The latter result is disputed by a recent DCA calculation by Alexandru Macridin, Mark Jarrell, Thomas Maier, P.R.C. Kent, *cond-mat/0509166*.

124. Kyle Shen, *Private communication*.

125. V. Hankevych, B. Kyung, A.-M. Daré, D. Sénéchal, and A.-M. Tremblay, in: *Proceedings of SNS2004* (2005), *J. Chem. Phys. Sol., in press, cond-mat/0407085.*

126. P.K. Mang, O.P. Vajk, A. Arvanitaki, J.W. Lynn, and M. Greven, *Phys. Rev. Lett.* **93**, 027002 (2004).

127. M. Matsuda, Y. Endoh, K. Yamada, H. Kojima, I. Tanaka, R.J. Birgeneau, M.A. Kastner, and G. Shirane, *Phys. Rev.* **B45**, 12548 (1992).

128. Y. Onose, Y. Taguchi, K. Ishizaka, and Y. Tokura, *Phys. Rev. Lett.* **87**, 217001 (2001).

129. M. Greven, *Private communication.*

130. Y. Onose, Y. Taguchi, K. Ishizaka, and Y. Tokura, *Phys. Rev.* **B69**, 024504 (2004).

131. H. Matsui, K. Terashima, T. Sato, T. Takahashi, S.-C. Wang, H.-B. Yang, H. Ding, T. Uefuji, and K. Yamada, *Phys. Rev. Lett.* **94**, 047005 (2005).

132. R.P.S.M. Lobo, N. Bontemps, A. Zimmers, Y. Dagan, R. Greene, P. Fournier, C. Homes, and A. Millis (*in press*).

133. A.J. Millis, A. Zimmers, R.P.S.M. Lobo, and N. Bontemps, *On the Optical Conductivity of Electron-Doped Cuprates,* in*: Mott Physics* (2004), *cond-mat/0411172.*

134. T. Hanaguri, C. Lupien, Y. Kohsaka, D. Lee, M. Azuma, M. Takano, H. Takagi, and J. Davis, *Nature* **430**, 1001 (2004).

135. C. Stock, W.J. L. Buyers, R. Liang, D. Peets, Z. Tun, D. Bonn, W.N. Hardy, and R.J. Birgeneau, *Phys. Rev.* **B69**, 014502 (2004).

136. M. Norman, D. Pines, and C. Kallin, *cond-mat/050731, Adv. Phys.* (*in press*).

137. P. Fournier, P. Mohanty, E. Maiser, S. Darzens, T. Venkatesan, C. Lobb, G. Czjzek, R. Webb, and R. Greene, *Phys. Rev. Lett.* **81**, 4720 (1998).

138. E. Motoyama, P. Mang, D. Petitgrand, G. Yu, O. Vajk, I. Vishik, and M. Greven, *unpublished*.

139. J. Sonier, K. Poon, G. Luke, P. Kyriakou, R. Miller, R. Liang, C. Wiebe, P. Fournier, and R. Greene, *Phys. Rev. Lett.* **91**, 147002 (2003).

140. J. Sonier, K. Poon, G. Luke, P. Kyriakou, R. Miller, R. Liang, C. Wiebe, P. Fournier, and R. Greene, *Physica* **408-410**, 783 (2004).

141. S. Wakimoto, R.J. Birgeneau, M.A. Kastner, Y.S. Lee, R. Erwin, P.M. Gehring, S.H. Lee, M. Fujita, K. Yamada, Y. Endoh et al., *Phys. Rev.* **B61**, 3699 (2000).

142. S. Wakimoto, J.M. Tranquada, T. Ono, K.M. Kojima, S. Uchida, S.-H. Lee, P.M. Gehring, and R.J. Birgeneau, *Phys. Rev.* **B64**, 174505 (2001).

143. T.A. Maier, M.S. Jarrell, and D.J. Scalapino, *The Structure of the Pairing Interaction in the 2D Hubbard Model* (2005), *cond-mat/0508361.*

144. M. Maple, *MRS Bulletin* **15**, 60 (1990).

145. R. Haslinger and A. Chubukov, *Phys. Rev.* **B67**, 140504 (2003).

146. F. Marsiglio, *cond-mat/0510649.*

147. G. Deutscher, A.F. Santander-Syro, and N. Bontemps, *Phys. Rev.* **B72**, 092504 (2005).

148. H. Molegraaf, C. Presura, D. van der Marel, P. Kes, and M. Li, *Science* **295**, 2239 (2002).

149. A. Santander-Syro, R. Lobo, N. Bontemps, Z. Konstatinovic, Z. Li, and H. Raffy, *Europhys. Lett.* **62**, 568 (2003).

150. M. Norman, M. Randeria, B. Janko, and J. Campuzano, *Phys. Rev.* **B61**, 14742 (2000).

151. B. Kyung, A. Georges, and A.-M. Tremblay, *Potential-Energy (BCS) to Kinetic-Energy (BEC)-Driven Pairing in the Attractive Hubbard Model* (2005), *cond-mat/0508645.*

152. M. Sutherland, D.G. Hawthorn, R.W. Hill, F. Ronning, S. Wakimoto, H. Zhang, C. Proust, E. Boaknin, C. Lupien, L. Taillefer et al., *Phys. Rev.* **B67**, 174520 (2003).

153. P. Anderson, *Present Status of the Theory of High-T_c Cuprates* (2005), *cond-mat/0510053.*

154. S. Allen, B. Kyung, D. Bergeron, V. Hankevych, and A.-M. Tremblay, *unpublished*.

155. D.M. Broun, P.J. Turner, W.A. Huttema, S. Ozcan, B. Morgan, L.R., W.N. Hardy, and D.A. Bonn, *In-Plane Superfluid Density of Highly Underdoped* $YBa_2Cu_3O_{6+x}$ (2005), *cond-mat/0509223.*

156. I. Herbut, *Private communication*.

157. M. Hettler, M. Mukherjee, M. Jarrell, and H. Krishnamurthy, *Phys. Rev.* **B61**, 12739 (2000).

158. R. Blankenbecler, D.J. Scalapino, and R.L. Sugar, *Phys. Rev.* **D24**, 2278 (1981).

159. M. Potthoff, *Eur. Phys. J. B (France)* **32**, 429 (2003).